Tutor/s

Dr. Javier Fernández González
Departament de Ciència de Materials i Química Física

Dr. Jose A. Calero Martínez
AMES Group Sintering S.A.

Grau de Química

Treball Final de Grau

Cooling rate effect on the microstructure of Fe-Cu-C alloy during continuous furnace sintering and their mechanical behaviour.
Efecte de la velocitat de refredament en la microestructura d'aliatges Fe-Cu-C en la sinterització en forn en continu i el seu potencial comportament en mecanitzat.

Laura Ros Campos
January 2025

UNIVERSITAT DE BARCELONA

B:KC Barcelona Knowledge Campus
Campus d'Excel·lència Internacional

En primer lloc, vull agrair als meus tutors, el Dr. Jose Antonio Calero Martínez i el Dr. Javier Fernández González, per l'oportunitat de fer aquest treball i per l'aprenentatge que he adquirit gràcies a ells. Vull agrair a tot l'equip d'AMES, sobre tot a la Jing, a l'Esteban, al Samuel i a l'Antonio per ensenyar-me les tècniques i el funcionament dels aparells i proporcionar-me suport continu durant el treball.

Finalment, vull agrair a la meva família per tot el suport rebut durant tota la carrera. Gràcies.

REPORT

IDENTIFICATION AND REFLECTION ON THE SUSTAINABLE DEVELOPMENT GOALS (SDG)

The Sustainable Development Goals (SDG) are universal goals to achieve fairness and health to the planet, its biosphere and its communities. The SDG are described in the 2030 Agenda, developed by the ONU. It is important that both public institutions, such as universities, and the private sector do their part in achieving these goals for the sustainability of the future.

There are 17 goals, which are grouped into 5 areas, the P's: People, Planet, Prosperity, Peace and Partnership. Among these goals, the ones that align with this project are Goal 8: Decent Work and Economic Growth and Goal 12: Responsible Consumption and Production, which are part of the Prosperity and Planet areas respectively.

Components manufactured at the same conditions on different furnaces displayed differences in their properties and microstructure. These differences increase machining time and costs, wasting materials and influencing the final cost of the product. This project was born to identify the cause of this phenomenon, to set the foundation for a larger study which could help reduce energy, tools and materials costs, targeting Goal 12, which would improve productivity, which is included in Goal 8.

Furthermore, AMES incorporates the SDGs in their Code of Conduct, which includes the ethics of the company and its employees, the environmental policies to reduce emissions and waste, and information about worker's rights and equality in the workplace.

CONTENTS

1. SUMMARY

60% of the total volume of structural components manufactured for the automotive industry, with the press and sinter technology, are composed of Fe-Cu-C. The Fe-Cu-C alloys provide desirable properties while being cost-effective and easily sinterable in continuous belt furnaces. The resulting microstructure consists of equilibrium structures: pro-eutectoid ferrite and pearlite, proportion dependent on the amount of carbon alloyed.

Among the many advantages the sintering technology offers, the ability to obtain a complex shape, before the sintering, reduces the need for post-sintering machining operations, sometimes even eliminating them.

Fe-Cu-C components that were sintered under the same conditions, in different furnaces with slightly different cooling rates, presented similar properties and have indistinguishable microstructures, however, they were found to behave differently in the machining processes, increasing the cost and the time inverted in these operations.

A study of the machining process would expend a significant amount of components, consuming a large amount of resources and time, for this reason, the following study was proposed. Three compositions of the iron copper carbon alloy, Fe-1.5%Cu-0.2%C, Fe-1.5%Cu-0.5%C and Fe-2%Cu-0.8%C; were sintered and cooled at four different rates, with the objective to carry out measurements of their mechanical properties and observe the microstructures, to find the possible variances that the cooling rates could cause before the machining process.

Cooling rates are given by the speed, in revolutions per minute, of the convectors used in the Rapid Cooling section of the sintering furnaces. The cooling rates proposed for this study are 300, 600, 900 and 1200 rpm.

Mechanical properties, such as tensile and yield strength, were measured by tensile testing. For a set of samples, the transverse rupture strength was measured. The macroscopic or bulk hardness of all samples was measured by indentation in the HRB scale. Furthermore, the sintered densities were calculated and the carbon contents of the alloys were checked by using a Carbon & Sulphur analyser. The microindentation hardness, or Vickers indentation hardness, was measured for the three compositions. In the Fe-1.5%Cu-0.5%C compositions, it was possible to differentiate between the two structures involved, pro-eutectoid ferrite and pearlite, which allowed to see the influence of the cooling rate in each.

The microstructure was observed through optical and electron microscopy, after cutting the test bars to mount, polish and etch metallographic samples. The micrographs were used to conduct image analyses for the Fe-1.5%Cu-0.5%C alloy, to find the amount of ferrite and pearlite formed at the slowest and the fastest cooling rates.

The conclusions of this study will determine how the cooling rate affects the behaviour of the alloys and could serve as the basis for a larger study involving machining operations.

Keywords: Cooling rate, Fe-Cu-C, powder metallurgy, sintering, mechanical properties, microstructure, microindentation hardness, ferrite, pearlite.

2. RESUM

El 60% del volum de components estructurals fabricats per la indústria automotriu, amb la tecnologia “press and sinter”, són de composició Fe-Cu-C. Els aliatges de Fe-Cu-C proveeixen propietats desitjables, sent rendibles i fàcilment sinteritzables en forns continus. Les microestructures resultants consisteixen en estructures d’equilibri: ferrita pro-eutectoide i perlita, la proporció depenent de la quantitat de carboni aliat.

Entre els avantatges que la tecnologia de sinterització ofereix, la capacitat de obtindré una forma complexa, abans de la sinterització, redueix la necessitat de processos de post-sinterització de mecanització, en alguns casos eliminant-los.

Els components de Fe-Cu-C sinteritzats sota les mateixes condicions, en forns amb lleugerament diferents velocitats de refredament, presentaven propietats similars i tenen microestructures indistingibles, tanmateix, es van visualitzar diferents comportaments en el procés de mecanització, incrementant el cost i el temps invertit en aquestes operacions.

Un estudi del procés de mecanitzat gastaria una quantitat significativa de components, consumint una gran magnitud de recursos i temps, per aquesta raó, el següent estudi va ser proposat. Tres composicions de l’aliatge ferro coure carbó, Fe-1.5%Cu-0.2%C, Fe-1.5%Cu-0.5%C i Fe-2%Cu-0.8%C; han sigut sinteritzades i refredades a quatre velocitats diferents, amb l’objectiu de prendre mesures de les propietats mecàniques i observar les microestructures, per poder trobar possibles variàncies que les velocitats de refredament poden causar abans del procés de mecanitzat.

Les velocitats de refredament venen donades per la velocitat, en revolucions per minut, dels convectors usats en la zona de refredament “Rapid Cooling” en els forns de sinterització. Les velocitats de refredaments proposades per aquest estudi han sigut 300, 600, 900 i 1200 rpm.

Les propietats mecàniques, com la resistència a la tracció i el límit elàstic, han sigut mesurades mitjançant assajos de tracció. Per un conjunt de mostres, s’ha mesurat la resistència a la flexió. La duresa macroscòpica de totes les mostres s’ha mesurat per indentació en l’escala HRB. A més, les densitats de sinterització han sigut calculades i el contingut de carboni dels aliatges han sigut comprovats utilitzant un analitzador de carboni i sofre. La duresa de microindentació, o la duresa Vickers, s’ha mesurat per les tres composicions. En la composició de Fe-1.5%Cu-0.5%C, s’ha pogut diferenciar entre les dues estructures involucrades, la ferrita pro-eutectoide i la perlita, el que ha permet veure la influencia de la velocitat de refredament en les dues.

La microestructura ha sigut observada per microscòpia òptica i electrònica, després de tallar les peces per muntar, polir i atacar químicament provetes metal·logràfiques. Les micrografies s’han usat per dur a terme anàlisis d’imatges per l’aliatge Fe-1.5%Cu-0.5%C, per trobar la quantitat de ferrita i perlita formades en les velocitats de refredament més lenta i més ràpida.

Les conclusions d’aquest estudi determinaran com la velocitat de refredament afecta el comportament dels aliatges, i podria servir com a base per un estudi més ampli involucrant operacions de mecanització.

Paraules clau: Velocitat de refredament, pulverimetal·lúrgia, sinterització, propietats mecàniques, microestructura, duresa de microindentació, ferrita, perlita.

3. INTRODUCTION

3.1. POWDER METALLURGY

Powder Metallurgy (PM) is the term referring to the sequence of processes, from powder obtention to sintering, which lead to a metallic component made from metal powder. PM encompasses various technologies, the most common being the press-and-sinter, in which the metal powders are shaped and compacted by pressing under high pressures into a precise die and sintered at a temperature below melting point, binding the metal particles together.

PM is widely used for the fabrication of automotive parts for the advantages the press-and-sinter technology offers. Pressing provides net-shape or near net-shape components that reduce any posterior machining processes needed, such as drilling, grinding or milling.[1] Sintered components contain porosity, which reduces their weight, dampens vibration and allows for self-lubrication. Furthermore, sintering allows compositions impossible to obtain through other methods such as melting. Sintering components have homogeneous microstructures and, therefore, isotropic properties.

The reduction of machining processes, added to the relative low material waste and energy consumption, makes PM the most cost-effective industrial method available.[2]

The steps of the press-and-sinter technology are as follows.

3.1.1. Mixing

Depending on the desired properties of the sintered component, the composition will differ and the proportions between powders will change. Lubricant, e.g., wax, must be added to the mixture for the posterior compacting of the green part to counter the frictional forces that can hinder the density.[3]

3.1.2. Compacting

The powder mixture is poured into a die cavity, with the negative shape of the component to be manufactured. This tooling is precise and durable. Then, a high uniaxial pressure is applied until the powder is compacted, obtaining a “green” part with a density influenced by the pressure used.[3]

3.1.3. Sintering

Sintering is the process of heating a material, at a temperature below the melting point of its main constituent, where the particles weld together, resulting in solid components with controlled and precise properties and dimensions. This process usually takes place in continuous furnaces, under strictly controlled conditions.[3]

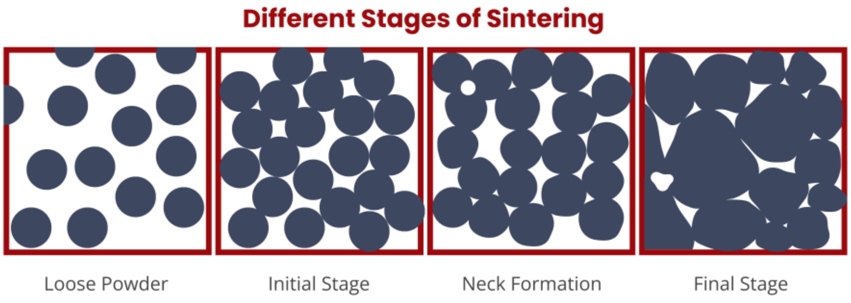

Figure 1: Sintering stages.[4]

As the compact is heated, alloying elements diffuse into the main metal. The grain size grows, and particles begin to bond through sintering necks, driven by the reduction of the interfacial energy.[5]

3.2. AMES

AMES is one of the world leaders involved in the manufacturing and sales of sintered metal components. AMES has production facilities through Spain, as well as in Hungary, USA and China, obtaining worldwide sales in over 50 countries. The main products include sintered structural parts for many industries, such as the automotive industry, electric and household appliances. As well as sintered gears, self-lubricating bearings, stainless steel parts, soft magnetic components and filters are also produced.

All these products are sintered in furnaces equipped with several control systems to monitor conditions and factors that influence on the final properties.[6]

3.2.1. Furnaces

The sintering process takes place in a continuous belt furnace, which is divided in the following sections: entrance, lubricant removal area, sintering, the rapid cooling, the cooling and the exit.

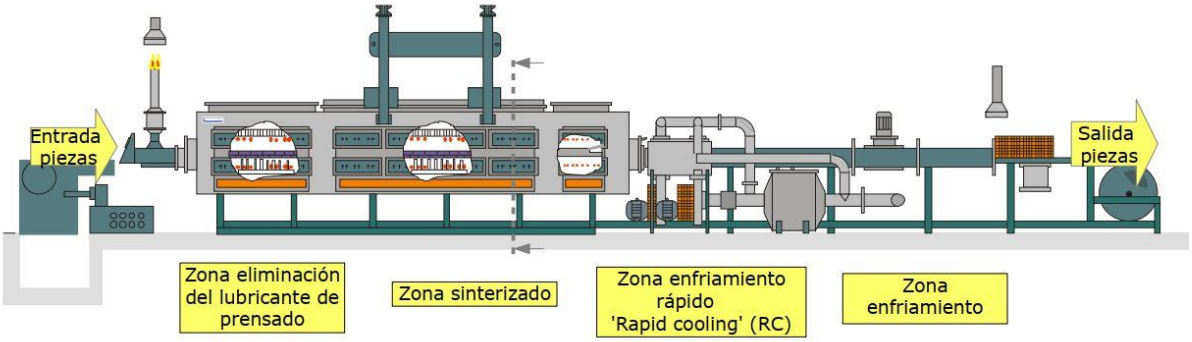

Figure 2: Continuous belt furnace.[7]

Entrance: The first section is where the green components are loaded into the belt, positioned in a way to avoid contact between the pieces. The belt will transport the pieces at the adequate speed for them to achieve the temperatures needed in the set times. The speed of the belt, sintering temperature and composition of the atmosphere are programmed beforehand to achieve the desired properties. The entrance, the Rapid Cooling and the exit are equipped with lambda sensors to monitor the oxygen level. The quantity of oxygen indicates the quality of the sintering process. Low amounts of oxygen are desired to avoid oxidation of the metal alloy. Oxides are considered an impurity and can decrease properties like hardness or tensile strength, as they limit the forming of bridges between the particles during sintering. [8]

Lubricant removal zone: The lubricant that was necessary in the pressing and compacting of the green components, now acts as a barrier between the metal particles that are supposed to bond when reaching the sintering temperature. Therefore, the lubricant must be burned before reaching the sintering zone. The de-lubricating temperature is set depending on the amount of lubricant and the material. The typical temperature reached is 600 ºC, which must be maintained during at least 15 minutes before reaching the pre-sintering temperature of 750-850ºC, to avoid blistering from the fast expansion of the lubricant. [8]

The atmosphere also plays an important role, it flows from the Rapid Cooling section to this one, dragging the evaporated products form the burnt lubricant. The gas atmosphere is necessary for uniform heat transfer and to avoid contact with the air. The composition depends on the material and its demands; however, most are a mixture of N_2 and H_2. Nitrogen is an inert gas, which protects the metal alloy from unwanted reactions. Hydrogen is a reducing agent that reacts with the metallic oxides that the powder particles have, as for Reaction 1, producing water vapor. Hydrogen aids in the lubricant removal step and prevents further oxidation.

$$Fe_xO_y + yH_2 \rightleftharpoons xFe + yH_2O \text{ (1)}$$

$$H_2 + \frac{1}{2}O_2 \rightleftharpoons H_2O \text{ (2)}$$

The atmosphere composition of 95% N_2 + 5% H_2 is the most common. However, if lubricant is not properly removed, sooting can occur, which is the deposition of carbon on the surface of the part, which affects the properties of the final product.

$$C + H_2O \longrightarrow CO + H_2 \text{ (3)}$$

Hydrogen can decarburize the component. The higher the hydrogen proportion is in the air, the more it will react with oxygen to form water, as for Reaction 2, which will react with the graphite on the sample, producing carbon monoxide, written in Reaction 3.

Sintering zone: After lubricant is removed, the green parts enter the sintering zone, the longest section of the furnace, where the highest temperature is reached. Many factors influence the sintering process.

Sintering temperature and time are key factors in the properties of the final piece. The sintering temperature influences on the diffusion and homogenization of the alloyed elements in the ferrous matrix. For example, carbon, at a sintering temperature of 1120ºC for 30 minutes, dissolves completely. At lower temperatures, some carbon can be left undissolved as free graphite depending on grain % and size, but by increasing the sintering time that graphite would dissolve into the iron lattice.[9]

The atmospheres used in this project were 95% N_2 + 5% H_2 and 94.7% N_2 + 5% H_2 + 0.3% NG. The natural gas (NG), consisting of a hydrocarbon mixture, acts as a source of carbon to counter major carbon losses. Hydrogen in the atmosphere and oxygen in the powder mixture participate in decarburization, adding gases such as methane aids in the recovery of the carbon content. The carbon content is crucial in both mechanical properties and final microstructure, thus, carbon control is required.

This zone is equipped with a sensor to measure the dew point, which is the temperature at which the water vapor in the air begins to condense, forming dew. It is measure of the ratio of hydrogen-to-moisture, which relates to the reduction capability. Hydrogen reduces the metal oxides, releasing water vapor. It is important to control this parameter, as a high dew point could affect the reduction capability of the atmosphere, having a negative impact on the final properties of the sintered part.[10]

Rapid Cooling and cooling zone: The sintered parts enter the Rapid Cooling area, sketched in Figure 3. It is equipped with four fans, labelled convectors since the method of cooling is by convective heat transfer. The atmosphere is the medium, which is previously cooled by heat exchangers. The convectors determine the speed of the atmosphere, higher speeds lead to faster cooling.

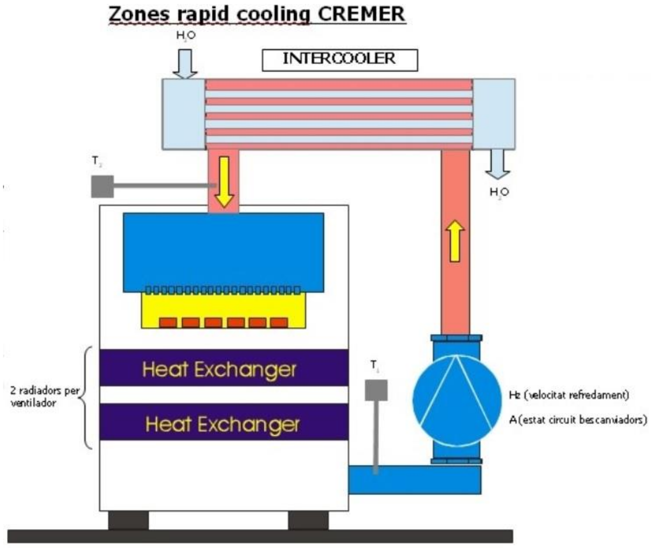

Figure 3: Sketch of Rapid Cooling area at AMES.[7]

Cooling rate, measured by the convector speed in rpm, determines the microstructure final component is made of. Slow cooling rates are used to obtain equilibrium structures, such as pearlite. The most common convector speeds used are 300 rpm and 1200 rpm, which is designated as "rapid cooling", being the fastest speed used.

Cooling rates influence the proportion of phases. The studied steels in this project have hypo-eutectoid (0.2%C and 0.5%C) and near eutectoid (0.8%C) compositions, so the two main allotropes of Fe involved are austenite, γ-Fe; and ferrite, α-Fe, which are represented in Figure 4, the iron-carbon phase diagram. The alloy of interest in this project is Fe-Cu-C, however, this diagram can be of use to describe the base behaviour of the phases.

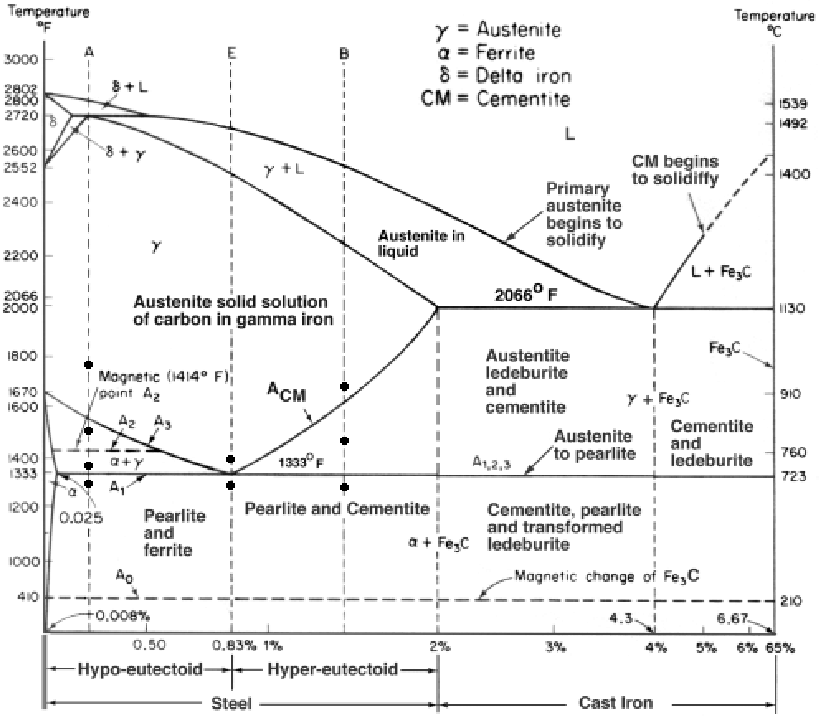

Figure 4: Fe-C phase diagram.[11]

At the lowest cooling rates, more time is given for carbon to diffuse at longer distances, resulting in the nucleation of coarser pro-eutectoid ferrite grains. As for the pearlite transformed from austenite, its eutectoid ferrite and cementite lamellas grow thicker.[9]

At faster cooling rates, the quantity of ferrite decreases, consequently increasing the quantity of pearlite. The nucleation rate of ferrite increases; however, the diffusion of carbon is hindered, as a result, ferrite grains are thinner and smaller than those cooled at lower rates. This leads to a lower percentage of pro-eutectoid ferrite in the final microstructure, since less time is spent in the α + γ region of the phase diagram. As for the pearlite, the eutectoid ferrite and cementite lamellas grow thinner with the increasing cooling rate.[9]

Pearlite is harder than ferrite, therefore, by applying faster cooling rates, the hardness and tensile strength of the alloy is increased.

Exit: The cooled parts exit the furnace, ready to head to further post-sintering processes such as machining.

A concern was raised for the sintering of the Fe-Cu-C alloy. Components of a determined composition, sintered, under the same conditions, in different furnaces with slight differences on the cooling rates presented the same properties and a similar microstructure. However, in the posterior machining, the components presented different behaviours, which increased the cost and the time of the machining operations, which slows down the production and rises the cost of the final piece. It is not known if the cooling rates used in the sintering furnaces at AMES influence significantly on the differences found in the machining, so a hypothesis of the cooling rate being the factor influencing this behaviour was raised. This study involves the use of four cooling rates to test their effects on the behaviour of the Fe-Cu-C alloy before the machining step, determining the properties and analysing the microstructure, which could help determine the effects of the cooling rates and save costs as well.

3.3. FE-CU-C

Iron-copper-carbon alloys are widely used in the PM industry for structural applications. Copper is a popular alloying agent. The melting point of copper is 1083 ºC, below the sintering temperature of the Fe-Cu-C alloy, which is typically 1120ºC.[12] The addition of copper strengthens the alloy, improving its mechanical properties, such as hardness and wear resistance; while being cost-effective. Carbon increases strength and hardness, while decreasing ductility.[13,14]

Carbon is insoluble in copper, but slightly soluble in iron. It has higher solubility in austenite, the FCC allotrope, than in ferrite, the BCC allotrope. Copper is soluble in iron; however, its solubility is hindered with higher concentrations of carbon. Furthermore, iron is also soluble in the molten copper.

Carbon undergoes interstitial diffusion, much faster than copper diffusion in iron, which is substitutional. To achieve complete absorption of copper in iron, hours at high temperatures are required. Meanwhile, for the dissolution of iron in molten copper, only a few minutes are needed.

In the sintering of Fe-Cu-C, as temperature raises, α-Fe transforms into γ-Fe and carbon starts to dissolve into it. When copper melts, it flows between the iron particles, penetrating grain boundaries and slowly dissolving into them, as illustrated in Figure 5. Some of the iron dissolves into the copper and precipitates, increasing the bonding between grains, resulting in coarser grains and a final lower number of grains.

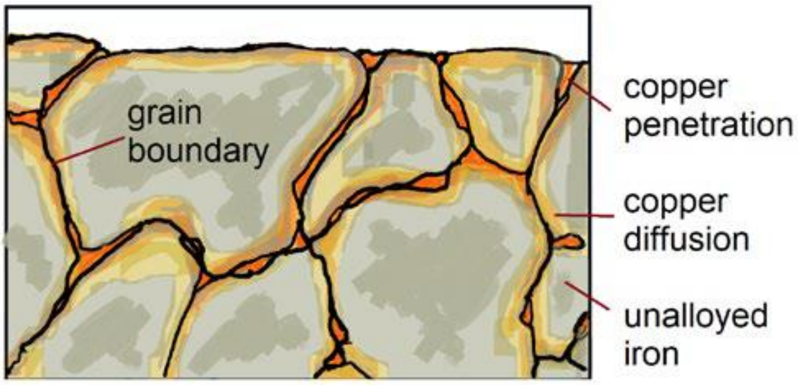

Figure 5: Copper distribution during the sintering of a powder compact.[12]

When the alloy is cooled, γ-Fe begins to transform into α-Fe and copper precipitates. At the eutectoid temperature of 723 ºC, the remaining austenite transforms into pearlite.[12]

4. OBJECTIVES

The main goal of this project is to determine how the cooling rate could affect the mechanical behaviour and microstructure of the Fe-Cu-C sintered alloy when an equilibrium phase microstructure is expected. Other objectives include using microindentation hardness to quantify the hardening of the microconstituents and conducting image analysis to find the percentages of the phases.

5. EXPERIMENTAL SECTION

5.1. MATERIALS AND METHODS

Three compositions of the Fe-Cu-C alloy were sintered, as described in Table 1.

Table 1: Compositions.

	Composition
R	Fe-1.5%Cu-0.2%C
T	Fe-1.5%Cu-0.5%C
S	Fe-2%Cu-0.8%C

Tensile test and Transverse Rupture Strength specimens were prepared following the MPIF Standard 60, with dimensions described in MPIF Standard 10. Fe powder was obtained from Rio Tinto, Cu powder from Pometon and graphite powder from Technografit. For lubrication, 0.6% of wax, from Münzing Chemie, was added to the powder mixtures.

R and S samples were sintered and cooled with four different cooling rates, as described in Table 2. The T samples were cooled at only the two extremes. The furnaces do not have a system to monitor the temperature in the cooling area; therefore, the cooling rates are expressed in revolutions per minute, which is the speed of the convectors.

Table 2: Cooling rates.

	i / 1	**ii**	**iii**	**Iv / 4**
Cooling rate	300 rpm	600 rpm	900 rpm	1200 rpm

The most used cooling rates are 300 rpm and 1200 rpm, the 1200 rpm speed is used for fast cooling. The other two, 600 rpm and 900 rpm, are rarely used and were proposed for the purpose of comparing the properties. All the samples were supposed to be sintered in the same furnace, to minimize the influence any factor other than the cooling rate could have on the properties and microstructure of the alloys.

However, for external reasons to this research, the last test pieces had to be sintered in a different furnace. To differentiate between them, samples sintered in the first furnace (HC-53) use roman numerals for the cooling rates and the samples sintered in the second one (HC-54) use arabic numerals.

5.2. PROPERTIES

5.2.1. Sintered Density

Density is a key factor in the properties of the alloy. Density has the most influence in the hardness of a sintered part, followed by carbon content and then copper content.[12] Density is related to the porosity; a higher density implicates a lower porosity. Knowing the density of the alloys becomes important to rightfully compare their properties when cooled at different rates. The samples were compacted at 600 MPa. Green densities, which is the density of the component before sintering, were not measured.

Density can be determined by knowing the weight and measurements of the sample piece. However, the shape and dimensions of the tensile test bars complicate measuring density in such a straightforward way. Instead, the sintered density was determined by the Archimedes method, following section 5 of MPIF Standard 42, determination of dry density.

As stated in the standard, if the sample contains porosity, which is the case for PM parts, it must be coated with paraffin before submerging it in water, avoiding the liquid to penetrate. The sintered density can be calculated following this formula, where ρ_w is the density of water at 22.0ºC.

$$\rho_s = \frac{(A\rho_w)}{(B-C)}$$

5.2.2. Carbon content

Carbon content crucially affects properties of PM steels, such as hardness, tensile properties and corrosion resistance; therefore, it is necessary to control it to ensure that no processes of decarburization occur prior or during the sintering. Having similar carbon contents in between batches cooled at different rates is important to carry out a correct comparison of their properties.

The carbon content was measured with the LECO CS230 Carbon & Sulphur analyser, following the MPIF Standard 66.

5.2.3. Bulk hardness

Hardness is the measure of the resistance of a material to localized plastic deformation, indentation, cutting, bending or scratching.

The hardness of an automotive component is key, as it affects the resistance, durability and performance under high-pressure conditions. These properties influence the behaviour of the parts and the safety of the vehicle they are used on.

The hardness was measured following the MPIF Standard 43. All measurements were taken using the Rockwell B scale, indenting the samples with a 1/16 ball indenter with an applied load of 100 kg, with the HR-400 Mitutoyo Rockwell Hardness Testing Machine.

For the tensile test bars, measurements were taken in the centre, spreading out the indentations in the width of the bar. For the test samples made for compression testing (TRS), measurements were also made in the centre of the piece; four indentations forming a square. Measurements made away from the middle varied depending on the site of the indentation, the thinner, more compact, side resulted in higher hardness values, and the thicker side resulted in lower hardness values.

5.2.4. Transverse Rupture Strength

The transverse rupture strength (TRS), or flexural strength, is the maximum stress a material can bear when bending before breaking. It was measured following the MPIF Standard 41, using the Shimadzu Autograph 100kN testing machine. Both tensile strength and TRS tends to increase with the amount of carbon in low alloyed steels.

5.2.5. Tensile Testing

Tensile testing is a destructive test to figure out how the material mechanically acts when tension is applied. It measures the deformation, known as elongation, of the test sample, caused from a controlled applied load. The result of the test shows the evolution of an applied load versus the put elongation; however, each value is divided by the cross-sectional area of the test bar to obtain the stress and by the fixed gauge to obtain the strain, ending with a stress versus strain curve with the same shape. Various properties can be found from the stress versus strain curve: the yield strength, the ultimate tensile strength and the percentage of elongation.

The yield strength is the stress at which plastic deformation begins. It is the end of the linear elastic region, as this deformation is irreversible, and strain increases faster than stress.[15]

The ultimate tensile strength (UTS) is the maximum stress a material can withstand without breaking. It is the highest point on the engineering stress-strain curve, where the slope is zero. However, on a true stress-strain curve, it wouldn't be the highest point. Necking occurs in the sample and the cross-sectional area decreases, but the engineering stress-strain curve assumes that the cross-sectional area of the tensile test sample is the same as the beginning, which makes the slope go downwards.

Elongation is the maximum length a material can reach before breaking. It is expressed as a percentage of the original length. A larger elongation percentage indicates higher ductility. It is inversely proportional to the other tensile properties.

Knowing the tensile properties of the parts is crucial to check if they are suited for their intended use.

Tensile tests for every batch were carried out using the Shimadzu Autograph 100kN testing machine and results were obtained through the Trapezium X software. Elongation was measured with an extensometer, with a gauge length of 30 mm.

5.2.6. Microindentation hardness

Microindentation hardness testing consists of applying a known load for a controlled period by pressing with a pyramidal diamond indenter. The Vickers indenter with a 100g load has been used for all three alloys, following the procedure described in the MPIF Standard 51, using the Shimadzu Microhardness Tester Type M.

The samples are indented after being chemically attacked, so that the microstructure is revealed, as to target the different microstructure constituents and check if there is a difference between the hardness of the phases when cooled at different rates.

For heterogeneous materials, such as the Fe-Cu-C alloy, the grain size, composition and boundaries affect the hardness readings. With macroindentation hardness, the indenter covers a larger area, as seen in Figure 6a, obtaining a better representation of the mean hardness. For microindentation hardness, the size of the indentation covers a smaller area, as seen in Figure 6b; therefore, differences in number of grains, grain size, type of grain and the boundaries between indentations cause variances in the hardness readings.[16]

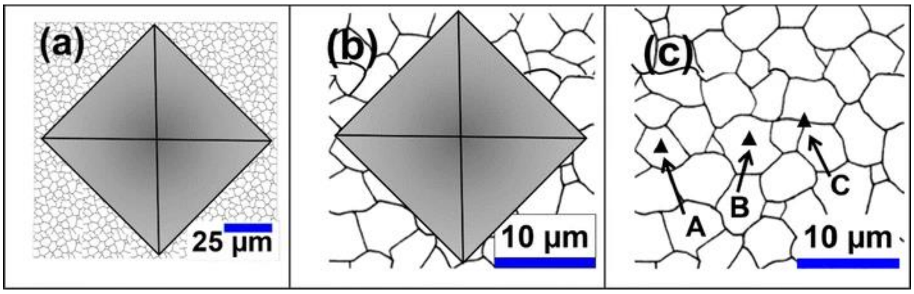

Figure 6: Indentations of a polycrystalline material at macroscale (a), microscale (b) and nanoscale (c).[16]

5.3. METALLOGRAPHY

To observe the microstructure, metallographic samples were prepared. Pieces from the centre of the test parts were cut with the Linear Precision Saw IsoMet 4000 and polished briefly to remove any burring. The metallographic samples were prepared with the Buehler SimpliMet 4000 Mounting System, using two types of bakelite resin, the EpoMet G Molding Compound and the Aka-Resin Phenolic from Akasel. The samples reach a pressure of 290 psi, are heated to 180ºC for 3.5 minutes and cooled for 3.67 minutes.

Then, the samples must be polished. Automated polishing was carried out with the MetaServ 250 Grinder-Polisher, where up to 6 samples could be polished at once. Manual polishing was carried out with the Buehler EcoMet 30 Manual Grinder-Polisher. For both methods, four polishing cloths were used.

First, samples are polished with a CarbiMet Silicon Carbide Grinding Paper, which must be new every time, with running water for 5 to 8 minutes at 300 rpm. Then, the grinding paper is switched to a VerduTex cloth, to polish the samples at 150 rpm with a LECO Premium Diamond Suspension of 6 micron for 8 to 10 minutes. With another VerduTex cloth, at the same speed and time, the samples are polished with a suspension of 3 micron. Finally, using a Lecloth Pad and an Alumina Polishing Suspension for 5 to 8 minutes at 500 rpm, the samples are polished and ready for the chemical attack.

To reveal the microstructure, the samples must be attacked with an acidic solution. There are many options available, depending on the composition of the alloy. For this study, 0.5% Nital was used (99.5 ml ethanol and 0.5 ml nitric acid). Not all samples were etched for the same amount of time, the R composition needed less seconds to be as etched as the S composition.

5.3.1. Optical Microscopy

The microstructures were observed through optical microscopy, using the Olympus GX51 Inverted Microscope and the Olympus Stream Essentials software. Micrographs were taken at different magnifications, from x110 to x2200. With the optical microscope, phases could be easily differentiated, however, the highest magnification is not enough to resolve clearly the pearlite microstructure. In pearlite, only the ferrite is attacked, the cementite, which is a carbide, is not attacked. When etched, the most attacked areas are the grain boundaries and the phase boundaries.

5.3.2. Scanning Electron Microscopy

Scanning Electron Microscopy (SEM) is a microscopy technique that uses a focused beam of electrons instead of light. Optical microscopy can only reach up to 200 nanometers of resolution meanwhile SEM can reach subnanometric resolutions (4-40 nm).

The backscattered electron (BSE) detector was used. BSE detector provides compositional information about the sample, as atoms with a lower atomic number, such as C; will appear lighter and atoms with relatively higher atomic numbers, such as Cu or Fe, appear slightly darker.[17] Furthermore, BSE provides topographic information.[18]

The samples observed through SEM must be conductive, for the electrons to interact with the surface of the sample. The metallic pieces are conductive; however, the resin of the metallographic sample may not be conductive. There are resins on the market specifically for preparations of SEM samples, like Buehler's KonductoMet, however, if the resin used is not conductive, copper wire can be used to connect the samples to the sample stage of the microscope. Micrographs were taken with the SEM Quanta 250 working at 20 kV at CCiTUB.

5.3.3. Image Analysis

Analysis of the obtained micrographs was carried out with the ImageJ 1.x software, a public domain Java-based image processing program, developed by Wayne Rasband in the National Health Institute. This program is free to use and can be ran online or downloaded for different platforms, where new features are uploaded constantly. A screenshot of the program is shown in Figure 7.

The method used for the analysis is: Load the image by clicking on File and Open. Set the scale drawing a line over the scale bar on the micrograph and clicking Analyze and then Set Scale, selecting global. Once done, crop the bar out. Then, convert the image by going into Process, Type and then 8-bit. Set the threshold by going into Image, Adjust and Threshold. Then measure the area covered by the threshold by going into Analyze, Analyze Particles and selecting Summarize.

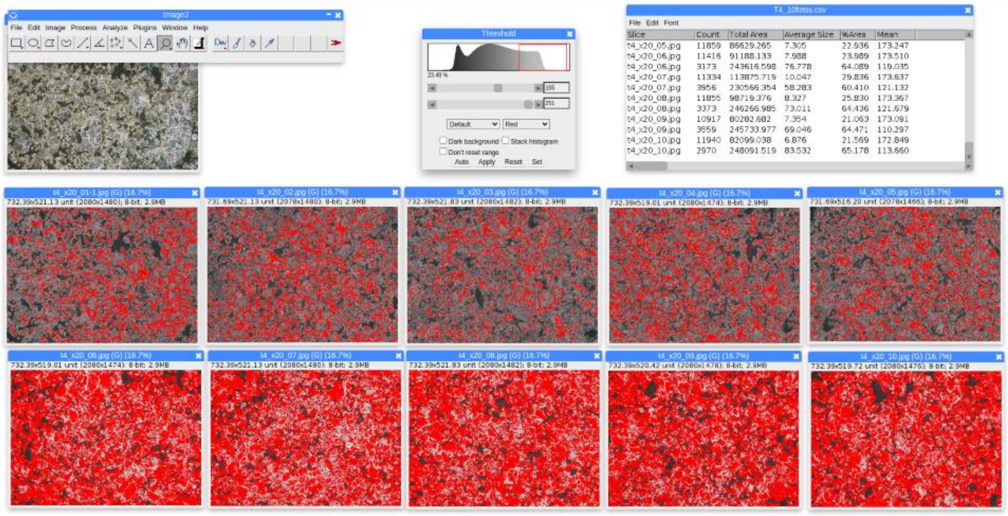

Slice	Count	Total Area	Average Size	%Area	Mean
t4_x20_05.jpg	11859	86629.265	7.305	22.936	173.247
t4_x20_06.jpg	11416	91188.133	7.988	23.989	173.510
t4_x20_06.jpg	3173	243616.598	76.778	64.089	119.035
t4_x20_07.jpg	11334	113875.719	10.047	29.836	173.637
t4_x20_07.jpg	3956	230566.354	58.283	60.410	121.132
t4_x20_08.jpg	11855	98719.376	8.327	25.830	173.367
t4_x20_08.jpg	3373	246266.985	73.011	64.436	121.679
t4_x20_09.jpg	10917	80282.682	7.354	21.063	173.091
t4_x20_09.jpg	3559	245733.977	69.046	64.471	110.297
t4_x20_10.jpg	11940	82099.038	6.876	21.569	172.849
t4_x20_10.jpg	2970	248091.519	83.532	65.178	113.660

Figure 7: Screenshot of ImageJ program, thresholds appear as a red mask over the micrographs.

It is important to remark that the obtained ferrite and pearlite quantities are relative; this analysis is approximate, since it depends on a threshold. For more accurate results, measurements could be made by drawing the pearlites by hand, however, this process is more time consuming. Additionally, a result can't be given from only one or a few micrographs. Even though the microstructure of the sintered pieces is homogeneous through the piece, the magnification makes the quantity of pearlite vary significantly between different micrographs of the same metallographic sample. Consequently, measurements must be taken from several micrographs.

However, one manual analysis could be conducted to set a threshold for the subsequential automated analyses. The pearlites could be selected by drawing the silhouettes, and then by using the "Analyze Particles" section, the percentage of pearlite would be obtained. Then, an automated analysis would be performed by setting the threshold at a value that results in the same percentage of pearlite. The threshold value, then, would be used for the other micrographs. Nevertheless, if the micrographs present different tonalities, e.g., pearlite is lighter or darker, this method does not work.

6. RESULTS AND DISCUSSION

6.1. PROPERTIES

6.1.1. Sintered Density

The sintered density was determined from the central pieces of the tensile test samples and from whole pieces of TRS samples. It is important as the density is higher in the middle of the tensile test bars. As for the TRS samples, determining density from one or the other half of the specimen will lead to significantly different density values, since one side is thicker than the other.

Table 3: Densities (g/cm³) of the different alloys (R, T, S) sintered in HC-53.

Cooling rate	**R**	**T**	**S**
i	6.87 ± 0.03	7.004 ± 0.008	6.92 ± 0.04
ii	6.84 ± 0.02	-	6.88 ± 0.02
iii	6.84 ± 0.01	-	6.87 ± 0.01
iv	6.83 ± 0.02	7.03 ± 0.05	6.87 ± 0.04

As seen in Table 3, densities are similar between cooling rates in the R and S compositions, except for the first rate, where it is higher.

Table 4: Densities (g/cm³) of the different alloys (R, T, S) sintered in HC-54.

Cooling rate	**R**	**T**	**S**
1	6.87 ± 0.01	6.92 ± 0.04	6.95 ± 0.06
4	6.93 ± 0.01	6.975 ± 0.003	6.98 ± 0.01

The density of at least four samples from each batch were measured. The densities seem to increase slightly between cooling rates in the three compositions, however, the variability between results in S and T samples practically makes them the same. R samples had more precise results.

6.1.2. Carbon content

The carbon content was measured from pieces lighter than 1.5 grams, which were broken with a hammer or cut with a hand saw. At least three pieces from different test samples were measured for each set of conditions and compositions. The lowest and highest carbon percentages measured of the samples, sintered in furnace HC-53, are expressed in Table 5.

Table 5: Carbon content (%) of the alloys (R, T, S) sintered in HC-53.

Cooling rate	**R** [%C]	**T** [%C]	**S** [%C]
i	0.193 - 0.201	0.422 - 0.425	0.732 - 0.753
ii	0.144 - 0.145	-	0.678 - 0.691
iii	0.135 - 0.141	-	0.702 - 0.734
iv	0.146 - 0.147	0.424 -0.440	0.687 -0.704

The carbon content of R and S samples cooled at 300 rpm (i) are significantly different from the rest. It is much higher than the samples cooled at 1200 rpm (iv), even though they were sintered at the same furnace, HC-53, with the same atmosphere, 95% N_2 + 5% H_2 + 0.3% GN. In Appendix 1, the sintering conditions of these batches of samples are shown. The sintering temperature and conveyor belt speed were also the same for both groups, the only difference is the level of O_2 in the Rapid Cooling section. It is not known why or how this variation occurred, as conditions were set the same.

As for the carbon contents measured from the samples sintered in HC-54, they present closer values between cooling rates, as seen in Table 6.

Table 6: Carbon content (%) of the alloys (R, T, S) sintered in HC-54.

Cooling rate	**R** [%C]	**T** [%C]	**S** [%C]
1	0.160 - 0.169	0.409 - 0.417	0.710 - 0.719
4	0.170 - 0.181	0.409 - 0.416	0.703 - 0.723

For the comparison of furnaces, the differences between the theoretical value of carbon for each composition (0.2%, 0.5% and 0.8%) and the lowest values measured were represented in Figure 8. Theoretically, a straight line should be expected, since cooling rate does not influence the carbon content, but affects the proportion of phases that form the structure of the alloys. Figure 9 represents the same differences excluding the slowest cooling rate, the trendlines show a near-zero slope, confirming the lack of influence cooling has on carbon percentage.

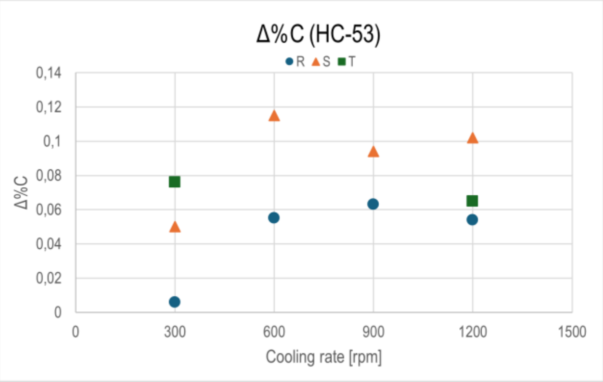

Figure 8: Differences of %C of R and S samples sintered in HC-53.

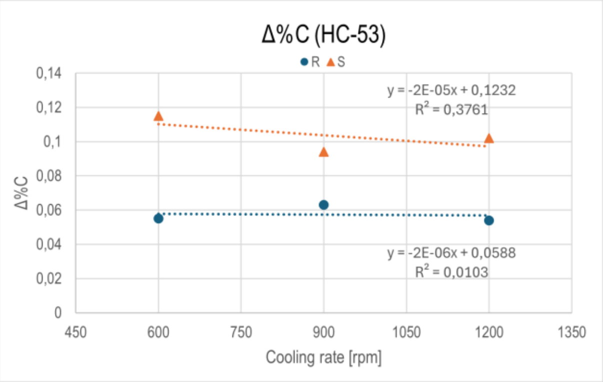

Figure 9: Differences of %C of R and S samples sintered and cooled at 600, 900 and 1200 rpm in HC-53.

Carbon contents of the samples sintered in HC-54 present closer values between cooling rates, as represented in Figure 10. It contrasts with the results of samples sintered in HC-53, which indicate that the first furnace, HC-54, offers more robust and repetitive results than the latter.

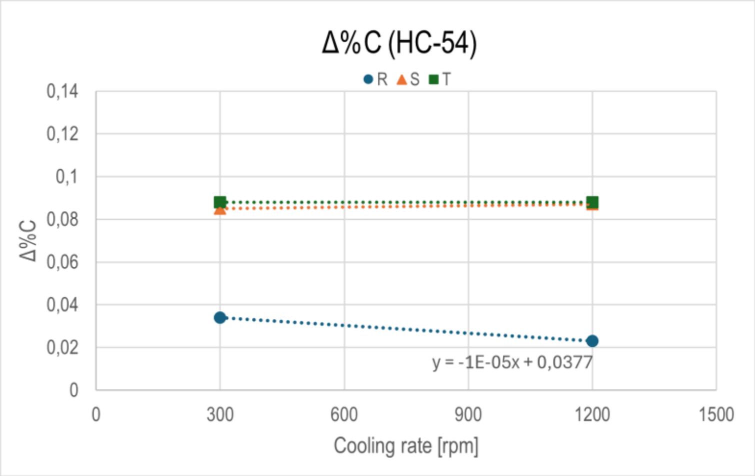

Figure 10: Differences of %C of R, T and S samples sintered in HC-54.

The differences are low enough to not influence significantly on the properties. Usually, differences in carbon content aren't as important, as clients ask for a range instead of a fixed number of carbon content, however, to research the influence of the cooling rate on the properties and microstructure of the proposed compositions, a stricter control is required.

6.1.3. Bulk hardness

Hardness was measured from at least four indentations in a sample, from at least three different samples in each condition and composition.

Table 7: Bulk hardnesses [HRB] of the different alloys (R, T, S) sintered in HC-53.

Sample	R [HRB]	T [HRB]	S [HRB]
i	57 ± 2	69 ± 2	86 ± 2
ii	51 ± 2	-	83 ± 2
iii	56 ± 3	-	85 ± 2
iv	59 ± 2	75 ± 2	84 ± 2

Table 8: Bulk hardnesses [HRB] of the different alloys (R, T, S) sintered in HC-54.

Sample	R [HRB]	T [HRB]	S [HRB]
1	60 ± 1	69 ± 2	87 ± 1
4	61 ± 2	72 ± 1	88 ± 1

The hardnesses obtained for samples sintered in both furnaces, represented in Table 7 and Table 8, correspond to what was expected, higher than the hardness of the 0.2%C pieces but lower than the 0.8%C pieces. The hardness is practically the same between the two cooling rates in the R and S samples and shows a slightly higher increase for the T samples. The effect of cooling rate on the macroindentation or bulk hardness isn't noticeable enough, reason to measure microindentation hardness instead.

The reason why T samples sintered in HC-53 have a bigger difference between cooling rates is because the TRS samples have a larger density and carbon content, as seen in Table 9, where the difference in hardness, as well as the average density and carbon content of the two cooling rates are expressed. Sintered hardness depends strongly on density, carbon content and copper content, in that order.[12]

Table 9: Difference in hardness, average density and carbon % of the T samples sintered in furnaces HC-53 (TRS) and HC-54 (Tensile).

	T in HC-53	T In HC-54
Δ Hardness [HRB]	6	3
Average Density [g/cm³]	7.02	6.95
Average %C	0.430	0.412

6.1.4. Transverse Rupture Strength

The transverse rupture strength from five T samples from each cooling rate was measured.

Table 10: Transverse Rupture Strength of T samples sintered in HC-53.

Sample	TRS [MPa]
Ti	910 ± 5
Tiv	970 ± 25

As seen in Table 10, there is a clear difference in the TRS of the samples cooled at different rates. Therefore, as the tensile properties do, the TRS increases with the cooling rate, resulting in components with higher strength.

6.1.5. Tensile Testing

For every condition, five sintered bars were subjected to tensile testing, except for the iv) condition, where the ten bars were used. Beforehand, the measurements of the thickness and width of the bars were taken. Most bars split at the centre, a few breaking closer to one end of the piece.

Table 11: Tensile properties of R samples sintered in HC-53.

Sample	**Yield Strength** [MPa]	**Tensile Strength** [MPa]	**Elongation** [%]
Ri	247.0 ± 0.9	319,7 ± 0.7	3.4 ± 0.1
Rii	245 ± 1	324 ± 2	5.0 ± 0.3
Riii	253 ± 3	334 ± 5	4.9 ± 0.6
Riv	252 ± 4	330 ± 4	4.1 ± 0.4

(a) Force 3-8 kN
(b) Yield strength at 0.2% offset to the nearest 1,000 psi (10 MPa).

The properties, represented in Table 11, display standard deviations that lead to appropriate RSD% values under 5%. First, an anomaly is noticed in the results for the elongation, which should be inversely proportional to the yield and tensile strengths, however the elongation for the slowest cooling rate is lower than expected. This is likely due to an error of the extensometer. For this reason, yield strength and tensile strength are the properties better suited to compare the influence of the cooling rate.

The yield strength and tensile strength slightly increases from the two slowest cooling rates, i and ii, to the two fastest cooling rates, iii and iv.

Table 12: Tensile properties of S samples sintered in HC-53.

Sample	**Yield Strength** [MPa]	**Tensile Strength** [MPa]	**Elongation** [%]
Si	448 ± 9	558 ± 3	1.39 ± 0.06
Sii	429 ± 11	554 ± 15	1.8 ± 0.1
Siii	481 ± 16	591 ± 13	1.5 ± 0.1
Siv	478 ± 5	576 ± 9	1.4 ± 0.1

These samples follow the same tendency as the R samples, the first condition is higher than it would be thought to be, and there is an increase for the values of yield strength and tensile strength from the ii (600 rpm) to the iii (900 rpm) condition, although more prominent than in the R samples, as seen in Figure 11 and Figure 12.

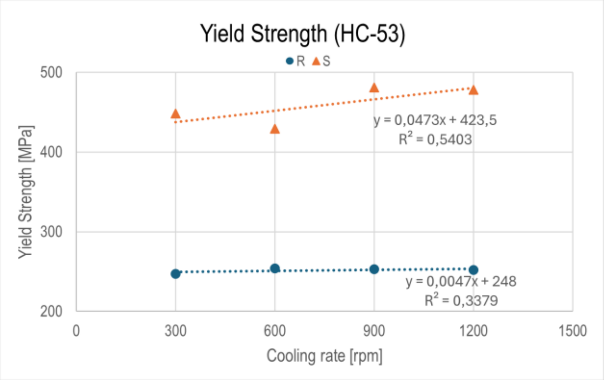

Figure 11: Yield Strength of R and S samples sintered in HC-53.

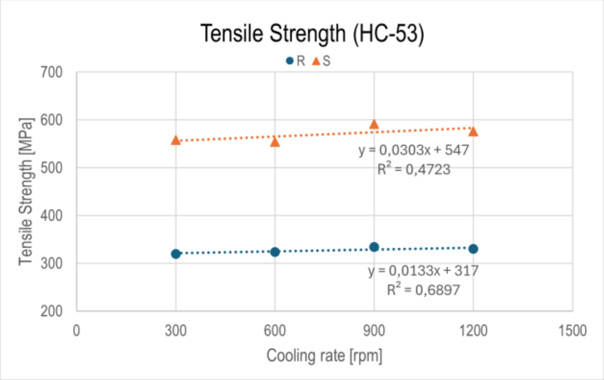

Figure 12: Tensile Strength of R and S samples sintered in HC-53.

The reason why the samples sintered at 300 rpm in furnace HC-53 present higher values than expected is due to the difference in carbon content, as shown in the previous section. Tensile properties depend on carbon content, as can be seen with the comparison of R and S samples (0.2%C and 0.8%C).

Tensile test samples of the three compositions, R, T and S; were sintered at the HC-54 furnace and cooled at the slowest and fastest cooling rates.

Table 13: Tensile properties of R samples sintered in furnace HC-54.

Sample	Yield Strength [MPa]	Tensile Strength [MPa]	Elongation [%]
R1	248 ± 2	321 ± 6	5.6 ± 1.6
R4	257 ± 7	328 ± 10	3.5 ± 0.3

Table 14: Tensile properties of T samples sintered in HC-54.

Sample	Yield Strength [MPa]	Tensile Strength [MPa]	Elongation [%]
T1	330 ± 5	438 ± 9	2.9 ± 0.5
T4	359 ± 3	466 ± 6	2.8 ± 0.1

Table 15: Tensile properties of S samples sintered in furnace HC-54.

Sample	Yield Strength [MPa]	Tensile Strength [MPa]	Elongation [%]
S1	469 ± 14	578 ± 10	1.4 ± 0.1
S4	499 ± 16	586 ± 20	1.2 ± 0.2

The three compositions follow the expected sequence of strength. First, R samples present the lowest strength because of the low carbon content, which was only 0.2%. T samples have intermediate strength, the carbon content having been raised to 0.5%C; and finally, S samples, which present the highest strength of all three, due to the 0.8% carbon and 2% copper contents. All three compositions show an increase of the yield strength and the tensile strength, as represented in Figures 13 and 14 respectively; as well as a decrease in the elongation.

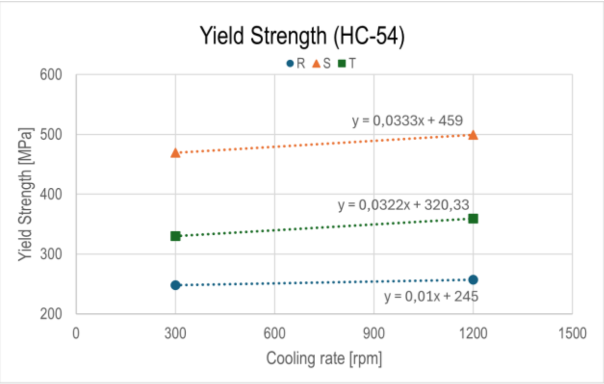

Figure 13: Yield Strength of R, S and T samples sintered in HC-54.

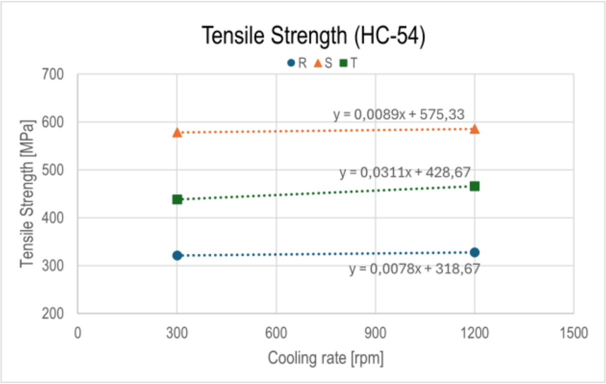

Figure 14: Tensile Strength of R, S and T samples sintered in HC-54.

6.1.6. Microindentation Hardness

A primarily ferritic structure is found in the 0.2%C alloy, with a small percentage of pearlite. Pearlite is scattered through the ferrite matrixes in such a way that indenting just ferrite with the indenter is almost impossible. The same problem arises with the 0.8%C alloy, as seen in Figure 15, where pearlite is the major microstructure constituent and ferrite is found among the pearlites. In consequence, hardness readings for the same microstructure vary depending on the zone of indentation.

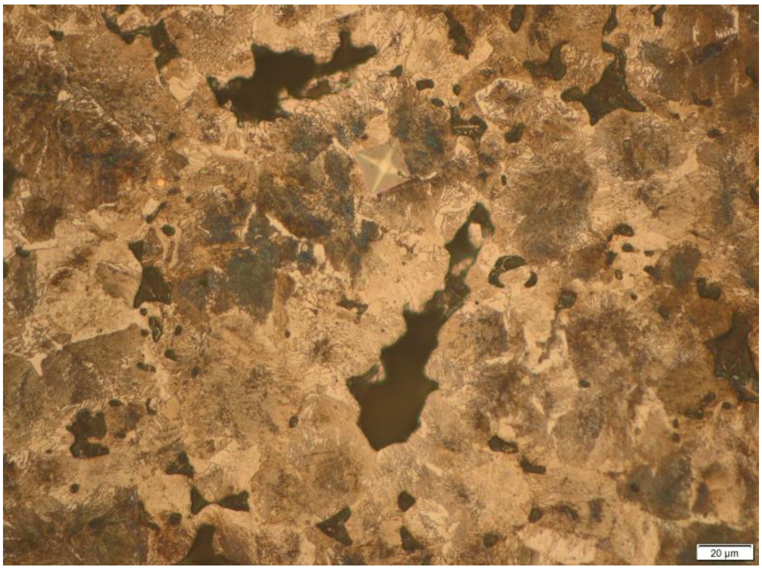

Figure 15: Vickers indentation in the 0.8C alloy (S).

This variation complicates the comparison of microindentation hardness (MH) between cooling rates. The possible difference wasn't expected to be high, since the bulk hardnesses measured for the different cooling rates were very similar, which was the reason why, instead of measuring the microhardness of the polished pieces, it was measured after the chemical attack, so that the microstructure could be revealed, and the phases could be targeted subsequently.

The results for the MH of R and S samples sintered in HC-53 are shown in Table 16, as expected, aren't very comparable. At first, the MH seems to increase slightly from the second slowest rate (ii, 600 rpm) to the fastest rate (iv, 1200 rpm). As happened with the other properties, the MH of the samples cooled at the slowest rate (i, 300 rpm) are higher than expected due to the abnormally "high" carbon content. However, the standard deviations show the variability of this measurement. Therefore, these MH values are considered to be in the same range and the cooling rate effect cannot be determined from these measurements.

Table 16: Microindentation Hardness [HV] of R and S samples.

Cooling rate	**R [**HV**]**	**S [**HV**]**
i	180 ± 18	330 ± 12
ii	170 ± 15	305 ± 19
iii	175 ± 17	310 ± 16
iv	178 ± 6	322 ± 24

Twenty to thirty measurements were taken for each sample. A high amount of MH tests must be conducted to obtain more representative average hardnesses, considering the distance between indentations, trying to avoid pores and edges and then discarding some measurements which might be too low or too high.

For the 0.5%C alloy, pearlite and proeutectoid ferrite are present in similar quantities, which makes the differentiation between them easier. This also facilitates measuring the hardness of the individual structures, as seen in Figure 16, where the indentation is on a pearlitic zone.

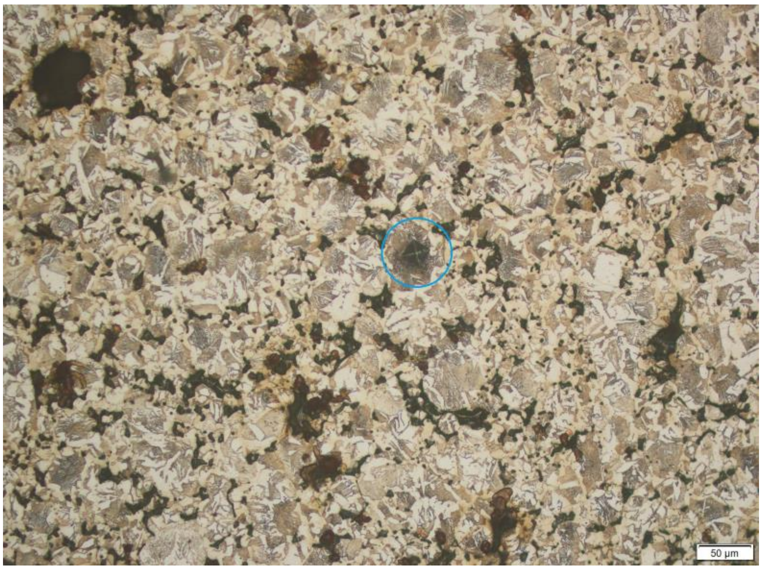

Figure 16: Vickers indentation in a pearlitic area in the 0.5%C alloy (T).

Table 17: Microindentation Hardness [HV] of ferrite and pearlite in the 0.5%C (T) samples.

Sample	**Ferrite [**HV**]**	**Pearlite [**HV**]**
Ti	176 ± 7	218 ± 10
Tiv	199 ±12	234 ± 9

The MH results for the T (Fe-1.5%Cu-0.5%C) are represented in Table 17. In contrast to R and S samples, the means and standard deviations don't overlap as much, as a higher number of measurements, sixty, were taken for each sample. An analysis of variance (ANOVA) concluded that the sets of measurements were different from each other, which is given in Appendix 2.

There are clear differences between ferrite and pearlite, as well as between the same structure cooled at different rates. The microindentation hardness of ferrite and pearlite increases with the increasing cooling rate.

6.2. METALLOGRAPHY

6.2.1. Optical Microscopy

The following figures show the microstructure of R (Fe-1.5%Cu-0.2%C) and S (Fe-2%Cu-0.8%C) cooled at different rates, taken from micrographs with a x1100 magnification.

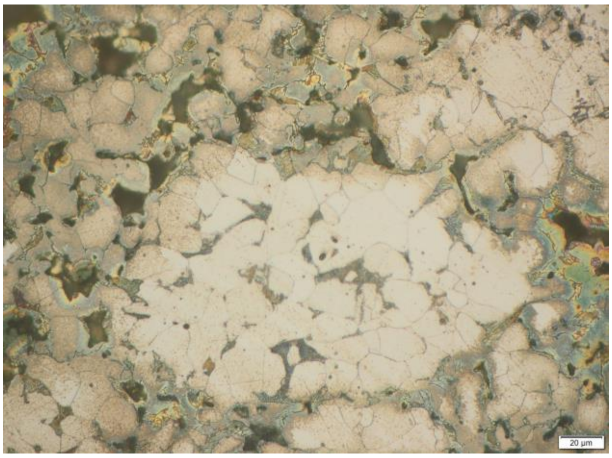

Figure 17: Micrograph of Ri (0.2%C at 300 rpm).

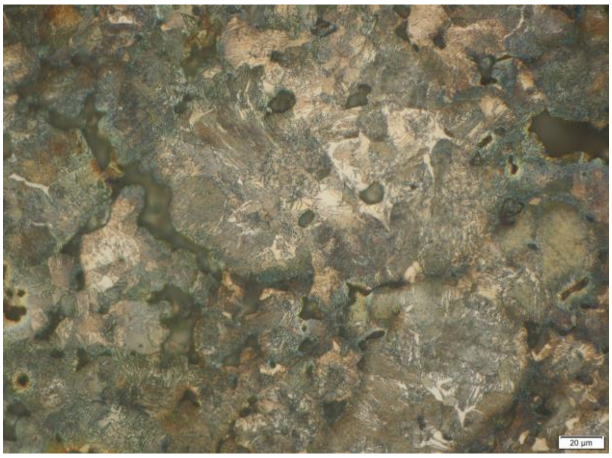

Figure 18: Micrograph of Si (0.8%C at 300 rpm).

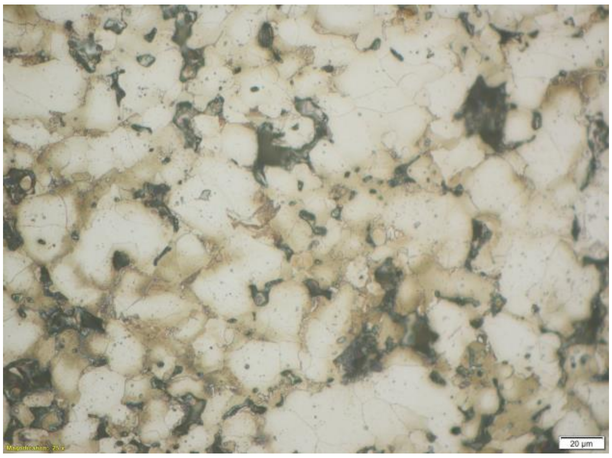

Figure 19: Micrograph of Rii. (0.2%C at 600 rpm).

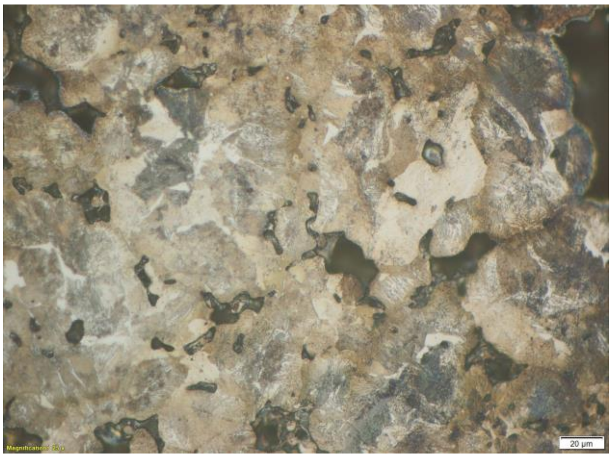

Figure 20: Micrograph of Sii. (0.8%C at 600 rpm).

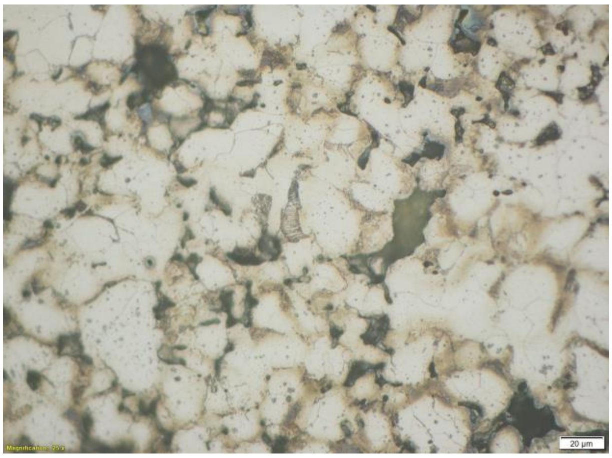

Figure 21: Micrograph of Riii (0.2%C at 900 rpm).

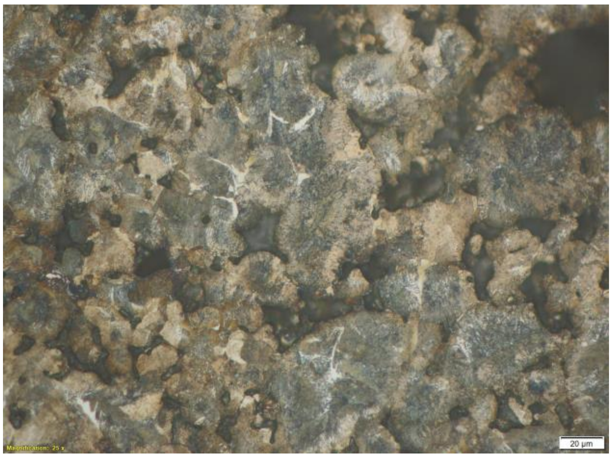

Figure 22: Micrograph of Siii (0.8%C at 900 rpm).

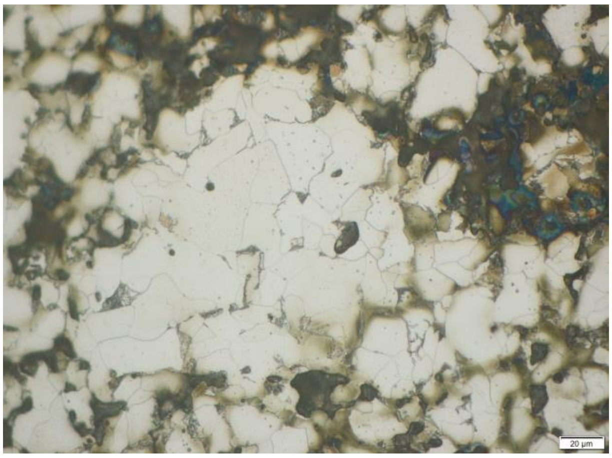

Figure 23: Micrograph of Riv (0.2%C at 1200 rpm).

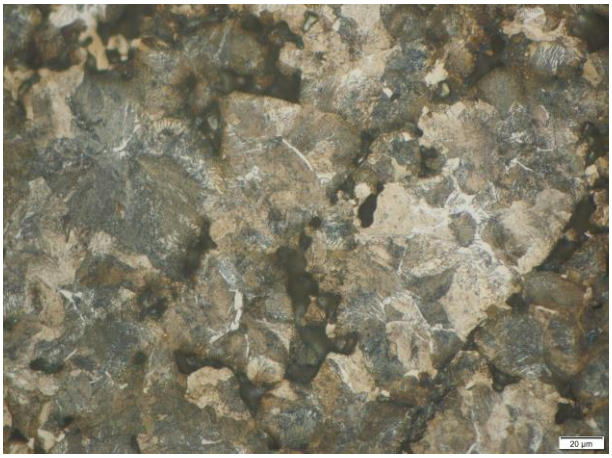

Figure 24: Micrograph of Siv (0.8%C at 1200 rpm).

Ferrite is seen as light and pearlite is dark. The brown borders at the grain boundaries is copper diffused in iron, which is a slow process. If the sintering time was increased, these borders would be broader. Areas like boundaries or defects are more likely to be attacked when etching. The topography of the creates a gradient of tonalities, as the amount of light collected by the microscope changes depending on the orientation of the grain.

The R microstructure is mostly ferrite, with small pearlite colonies. The copper diffusion in ferrite is visible. As seen in Figure 17 and Figure 23, pearlites that are near pores are more susceptible to etching.

The S microstructure is mostly pearlitic, as it is near the eutectoid composition, the real carbon contents of the alloys being around are 0.70%-0.75%C. Figure 20 appears lighter than the other three micrographs of the S samples because this area has been less etched. In this figure, the different tonalities of the pearlite grains can be seen.

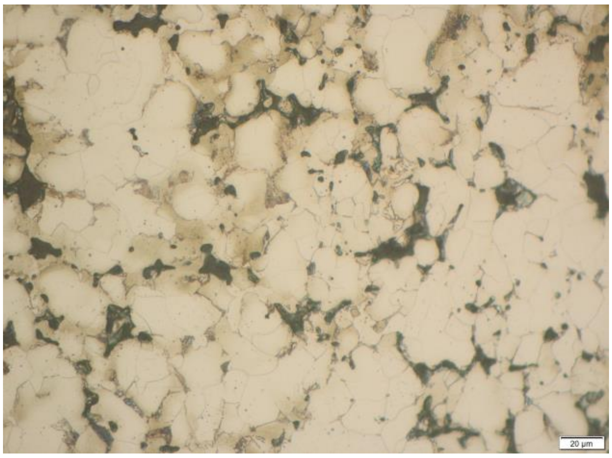

Figure 25: Micrograph of R1.

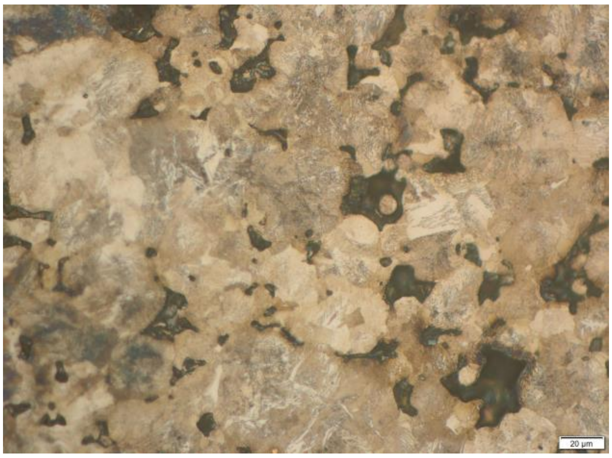

Figure 26: Micrograph of S1.

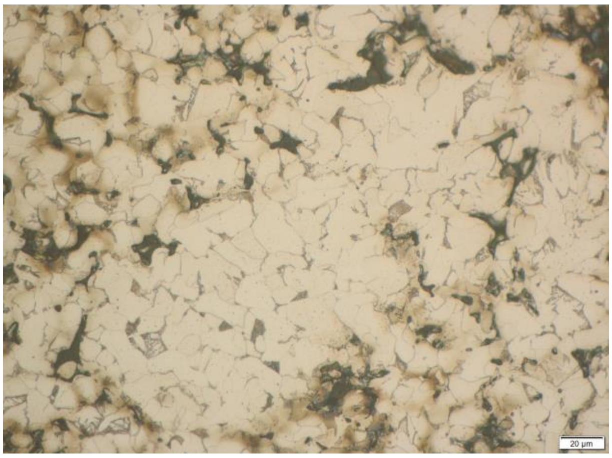

Figure 27: Micrograph of R4.

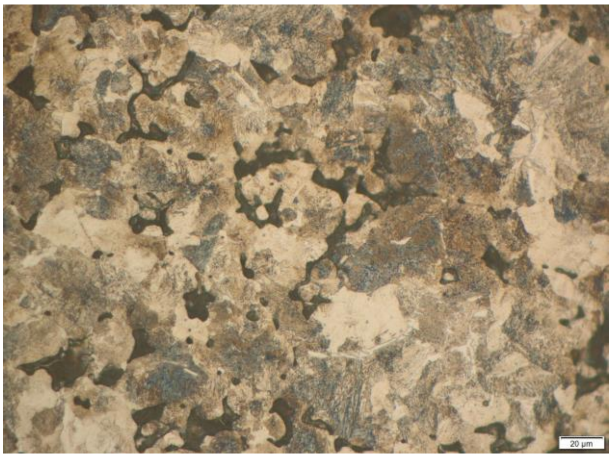

Figure 28: Micrograph of S4.

Figures 25-28 show the micrographs of R and S samples sintered in HC-54. There aren't notable differences between these samples and the samples sintered in HC-53 (i-iv).

For the T composition, Fe-1.5%Cu-0.5%C, an approximately equal proportion of ferrite and pearlite is observed.

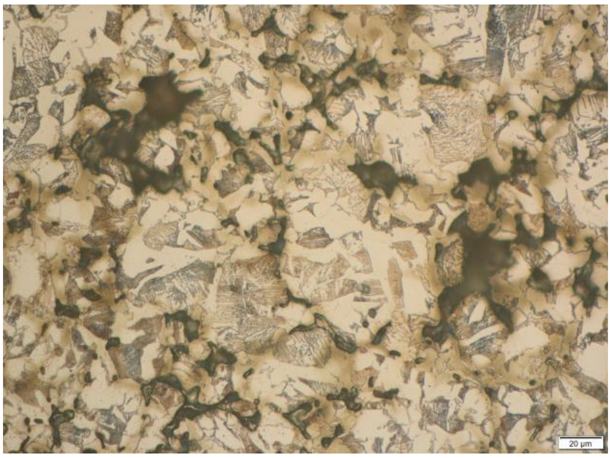

Figure 29: Micrograph of T1.

Figure 30: Micrograph of T4.

The pearlite content seems to increase from sample T1, Figure 29, to sample T4, Figure 30. To confirm this, image analysis involving several micrographs at 440x magnification is carried out.

6.2.2. Scanning Electron Microscopy

SEM allows the differentiation of ferrite and cementite in the pearlite colonies. Ferrite is darker and cementite is lighter. The following figures are SEM micrographs of R, T, and S alloys. Micrographs were taken for each cooling rate but no significant difference was found in between cooling rates. Appendix 3 contains additional micrographs from optical microscopy and SEM.

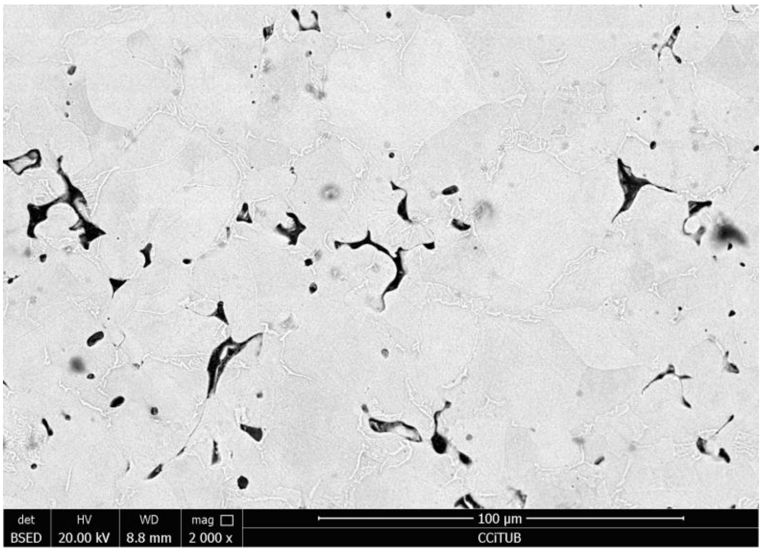

Figure 31: SEM Micrograph of Ri. (0.2%C at 300 rpm)

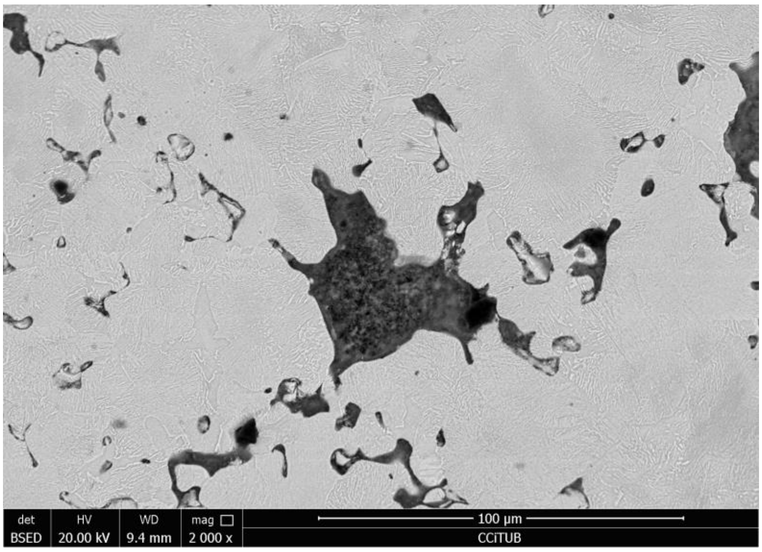

Figure 32: SEM Micrograph of Si. (0.8%C at 300 rpm)

The composition of “stain” in the middle of Figure 32 was analysed and the results are given in Table 18. It is an oxide, which could have resisted deoxidation in the sintering process.

Table 18: Composition by Weight% and Atom% of the "stain" in the S sample cooled at 300 rpm.

	C	O	Si	Ca	Fe	Cu
Weight %	10.47	26.09	2.14	0.74	55.85	4.71
Atom %	23.75	44.42	2.07	0.50	27.24	2.02

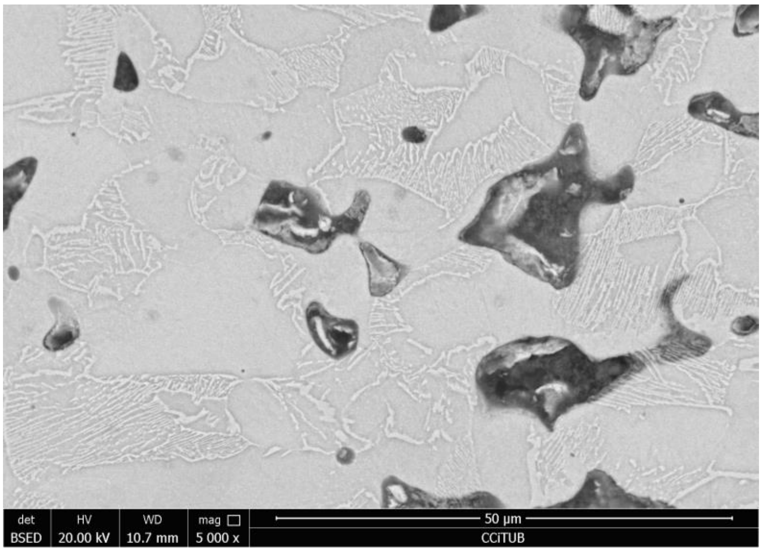

Figure 33: Micrograph of T sample, cementite is white, ferrite is light grey.

6.2.3. Image Analysis

Analyses were carried out for the T composition. Twenty micrographs were taken with the 20x objective lens and 22x optical lens, resulting in a x440 magnification. For the T samples cooled at 1200 rpm, the analysis was straightforward, as the microstructure of the metallographic sample had been homogeneously etched, therefore, the threshold set had remained constant. On a scale from 0 to 255, the range for pearlite was 72-165 and the range for ferrite 165-255.

Table 19: Ferrite and pearlite percentages measured for T4 micrographs.

T4 (1200 rpm)	% Ferrite	% Pearlite
Lowest and Highest values	22-34	66-78
Average	**28 ± 2**	**72 ± 3**

For the T samples cooled at 300 rpm, micrographs weren't that similar. Despite etching the metallographic sample for the same amount of time in the same exact manner, some areas of the sample were less etched, pearlite displaying lighter hues and some were more etched, pearlite appearing darker. Consequently, different thresholds had to be set, which are divided into three groups: A, B and C.

Table 20: Ferrite and pearlite percentages measured for T1 micrographs.

T1 (300 rpm)	Threshold	% Ferrite	% Pearlite
A	92-183	40-45	55-60
B	75-158	41-44	59-56
C	71-176	43-46	54-57
Average	-	**43 ± 2**	**57 ± 3**

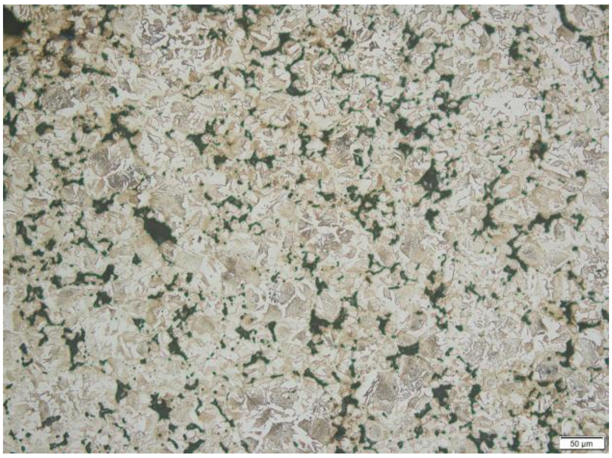

Figure 34: Micrograph of T1 sample, belonging to group A.

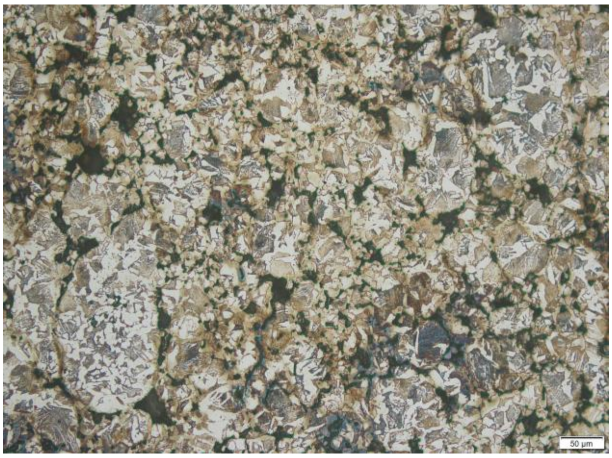

Figure 35: Micrograph of T1 sample, belonging to group B.

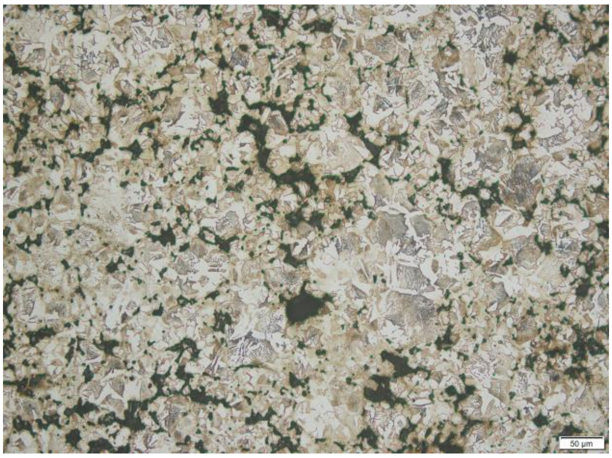

Figure 36: Micrograph of T1 sample, belonging to group C.

Table 21: Ferrite and pearlite percentages.

Sample	% Ferrite	% Pearlite
T1 (300 rpm)	43	57
T4 (1200 rpm)	28	72

a) The percentages are expressed taking the sum of pearlite and ferrite as 100%.
b) Standard deviations are 2% for T1 and 3% for T4.

As seen in Table 21, the quantity of ferrite decreases and the quantity of pearlite increases with the increasing cooling rate. Pearlite is harder than ferrite. This is important, because variations in the microstructure influence the machinability.[19]

7. CONCLUSIONS

The cooling rate affects tensile properties of the Fe-Cu-C alloy. Increasing the cooling rate leads to an increase in tensile and yield strength. Differences in the macroscopic hardness of the alloy, measured in the Rockwell B scale, were expected as well, however average values were similar.

As for the microindentation hardness, the effect of the cooling rate is observed more clearly. The microindentation hardness of ferrite and pearlite increase with the increasing cooling rate, measured for the Fe-1.5%Cu-0.5%C (T) composition. For the two other compositions, Fe-1.5%Cu-0.2%C (R) and Fe-2%Cu-0.8%C (S), the differentiation between the two structures wasn't possible. Nanoindentation, although it was not available in this project, could lead to a clearer differentiation between cooling rates for these two compositions.

The sintered density and the carbon percentage are not affected by the different cooling rates.

Cooling rate affects proportion of ferrite and pearlite. Less pro-eutectoid ferrite, and therefore more pearlite, are formed at faster cooling rates. The average percentages of ferrite and pearlite for the Fe-1.5%Cu-0.5%C composition (T) were found by analysing the micrographs, taken with the optical microscope, with the image processing software, ImageJ. The R and S compositions are harder and more time-consuming to analyse, as they require larger magnifications to differentiate the phases well, and, therefore, a big amount of micrographs are needed to obtain representative average values. R and S alloys present the same tendencies in their properties as T, so it could be assumed that cooling rate also affects the proportion of ferrite and pearlite, although probably at a smaller magnitude.

Since the microstructure and the mechanical properties of alloys, which were influenced by the different cooling rates, affect the machinability of the component, the proposed cooling rates will lead to differences in the machining operations. A subsequent study involving the machining process could be conducted, to determine how the cooling rate quantitatively affects the machining, by seeing the relation between the measured mechanical properties and the behaviour in the machining process.

8. REFERENCES AND NOTES

1. AMES Sintering: Complementary Manufacturing Operations. https://ames-sintering.com/complementary-manufacturing-operations/. (accessed Dec 27, 2024).
2. Why Powder Metallurgy. *PM Review* https://www.pm-review.com/introduction-to-powder-metallurgy/why-powder-metallurgy/. (accessed Dec 08, 2024).
3. AMES Sintering: Basic Manufacturing Process. https://ames-sintering.com/basic-manufacturing-process/. (accessed Dec 27, 2024).
4. Acedera, R. A. CAPLINQ BLOG: Different-Stages-of-Sintering. https://blog.caplinq.com/why-are-graphitized-carbon-panels-cheaper-than-sintered-titanium-for-gas-diffusion-layers_4138/different-stages-of-sintering/. (accessed Jan 03, 2025).
5. Kang, S. J. L. *Sintering: Densification, Grain Growth and Microstructure*. *Sintering: Densification, Grain Growth and Microstructure* (2005). doi:10.1016/B978-0-7506-6385-4.X5000-6.
6. AMES Sintering: About AMES. https://ames-sintering.com/about-ames/. (accessed Dec 18, 2024).
7. *AMES Internal Document.*
8. Coble, Scot. E. The impact of complete lubricant removal on the mechanical properties and production of PM components. (2022).
9. *Höganäs Handbook for Sintered Components Metallography*. vol. 6 (Höganäs AB, 2015).
10. He, L., Zurecki, Z., Bowe, D. & Ghosh, R. Continuous Dew Point Monitoring System for a Sintering Furnace. *AM&P Technical Articles* **174**, (2016).
11. Iyer, N. R. Behaviour of Heated and Naturally Cooled Steel Tubular Joints. in *National Conference on Fire Research and Engineering* (2014).
12. German, R. M. A review of the sintering of iron-copper-carbon alloys for structural Powder Metallurgy applications. *Powder Metallurgy Review* **12**, 69–96 (2023).
13. Wong-Ángel, W. D., Téllez-Jurado, L., Chávez-Alcalá, J. F., Chavira-Martínez, E. & Verduzco-Cedeño, V. F. Effect of copper on the mechanical properties of alloys formed by powder metallurgy. *Mater Des* **58**, (2014).
14. Nekatibeb, F., Raja Annamalai, A. & Upadhyaya, A. Effect of copper and graphite addition on sinterability of iron. *Transactions of the Indian Institute of Metals* **64**, (2011).
15. Iowa State University Center for Nondestructive Evaluation. Tensile Properties. *Physiscs of Nondestructive Evaluation* (2024). https://www.nde-ed.org/Physics/Materials/Mechanical/Tensile.xhtml (accessed Dec 03, 2024).
16. Broitman, E. Indentation Hardness Measurements at Macro-, Micro-, and Nanoscale: A Critical Overview. *Tribology Letters* vol. 65 Preprint at https://doi.org/10.1007/s11249-016-0805-5 (2017).
17. Zhou, W., Apkarian, R., Wang, Z. L. & Joy, D. Fundamentals of scanning electron microscopy (SEM). in *Scanning Microscopy for Nanotechnology: Techniques and Applications* (2007). doi:10.1007/978-0-387-39620-0_1.
18. What is Scanning Electron Microscopy? Scanning electron microscope technology explained. https://www.thermofisher.com/es/es/home/materials-science/learning-center/applications/what-is-scanning-electron-microscopy.html. (accessed Nov 28, 2024).
19. Genculu, S. Factors Affecting Machinability of Metals. *CAB Inc* (2015).

9. ACRONYMS

PM: Powder Metallurgy

FCC: Face-centered cubic

BCC: Body-centered cubic

UTS: Ultimate Tensile Strength

TRS: Transverse Rupture Strength

SEM: Scanning Electron Microscopy

MH: Microindentation Hardness

APPENDICES

APPENDIX 1: SINTERING CONDITIONS

Table 22: Sintering conditions of Ri and Si samples.

Furnace: HC-53	**Date: 26/09/2024**
10 samples Ri and 10 samples Si	
Sintering Temperature (ºC)	1120
Atmosphere	95% N_2 + 5% H_2 + 0.3% GN
Conveyor belt speed (m/h)	10
Convector rate (rpm)	**300**
Lambda sensors (mV)	O_2 level at entrance: 1070
	O_2 level at Rapid Cooling: 723
	O_2 level at exit: 1157
Dew point (ºC)	Sintering: 2.6 Rapid Cooling: -15.5

Table 23: Sintering conditions of Riv and Siv samples.

Furnace: HC-53	**Date: 04/10/2024**
10 samples Riv and 10 samples Siv	
Sintering Temperature (ºC)	1120
Atmosphere	95% N_2 + 5% H_2 + 0.3% GN
Conveyor belt speed (m/h)	10
Convector rate (rpm)	**1200**
Lambda sensors (mV)	O_2 level at entrance: No lecture.
	O_2 level at Rapid Cooling: 1125
	O_2 level at exit: 1170
Dew point (ºC)	Sintering: 2.0 Rapid Cooling: -17

Table 24: Sintering conditions of Ti samples.

Furnace: HC-53	**Date: 18/10/2024**
10 samples Ti	
Sintering Temperature (ºC)	1120
Atmosphere	95% N_2 + 5% H_2
Conveyor belt speed (m/h)	10
Convector rate (rpm)	600
Lambda sensors (mV)	O_2 level at entrance: No lecture.
	O_2 level at Rapid Cooling: 1115
	O_2 level at exit: No lecture.
Dew point (ºC)	Sintering: No lecture. Rapid Cooling: -10

Table 25: Sintering conditions of Rii and Sii samples.

Furnace: HC-53	**Date: 22/10/2024**
10 samples Rii and 10 samples Sii	
Sintering Temperature (ºC)	1120
Atmosphere	95% N_2 + 5% H_2
Conveyor belt speed (m/h)	10
Convector rate (rpm)	600
Lambda sensors (mV)	O_2 level at entrance: No lecture.
	O_2 level at Rapid Cooling: No lecture.
	O_2 level at exit: No lecture.
Dew point (ºC)	Sintering: No lecture. Rapid Cooling: No lecture.

Table 26: Sintering conditions of Tiv samples.

Furnace: HC-53	**Date: 31/10/2024**
10 samples Tiv	
Sintering Temperature (ºC)	1120
Atmosphere	95% N_2 + 5% H_2
Conveyor belt speed (m/h)	10
Convector rate (rpm)	1200
Lambda sensors (mV)	O_2 level at entrance: No lecture.
	O_2 level at Rapid Cooling: 1120
	O_2 level at exit: 1170
Dew point (ºC)	Sintering: No lecture. Rapid Cooling: -13

Table 27: Sintering conditions of Riii and Siii samples.

Furnace: HC-53	**Date: 31/10/2024**
10 samples Riii and 10 samples Siii	
Sintering Temperature (ºC)	1120
Atmosphere	95% N_2 + 5% H_2
Conveyor belt speed (m/h)	10
Convector rate (rpm)	900
Lambda sensors (mV)	O_2 level at entrance: No lecture.
	O_2 level at Rapid Cooling: 1123
	O_2 level at exit: 1173
Dew point (ºC)	Sintering: No lecture. Rapid Cooling: -14

Table 28: Sintering conditions of Rii and Sii samples.

Furnace: HC-54	**Date: 21/11/2024**
10 samples R4 and 10 samples S1	
Sintering Temperature (ºC)	1120
Atmosphere	95% N_2 + 5% H_2
Conveyor belt speed (m/h)	10
Convector rate (rpm)	300
Lambda sensors (mV)	O_2 level at entrance: No lecture.
	O_2 level at Rapid Cooling: 1175
	O_2 level at exit: 1134
Dew point (ºC)	Sintering: -31 Rapid Cooling: No lecture.

Table 29: Sintering conditions of R4 and S4 samples.

Furnace: HC-54	**Date: 22/11/2024**
10 samples R4 and 10 samples S4	
Sintering Temperature (ºC)	1120
Atmosphere	95% N_2 + 5% H_2
Conveyor belt speed (m/h)	10
Convector rate (rpm)	1200
Lambda sensors (mV)	O_2 level at entrance: No lecture.
	O_2 level at Rapid Cooling: 1138
	O_2 level at exit: 1145
Dew point (ºC)	Sintering: -35 Rapid Cooling: No lecture.

Table 30: Sintering conditions of T4 samples.

Furnace: HC-54	**Date: 04/12/2024**
10 samples T4	
Sintering Temperature (ºC)	1120
Atmosphere	95% N_2 + 5% H_2
Conveyor belt speed (m/h)	10
Convector rate (rpm)	1200
Lambda sensors (mV)	O_2 level at entrance: No lecture.
	O_2 level at Rapid Cooling: 1206
	O_2 level at exit: 1278 ± 2
Dew point (ºC)	Sintering: -31 ± 1 Rapid Cooling: No lecture.

Table 31: Sintering conditions of T1 samples.

Furnace: HC-54	**Date: 10/12/2024**
10 samples T1	
Sintering Temperature (ºC)	1120
Atmosphere	95% N_2 + 5% H_2
Conveyor belt speed (m/h)	10
Convector rate (rpm)	300
Lambda sensors (mV)	O_2 level at entrance: No lecture.
	O_2 level at Rapid Cooling: 1137
	O_2 level at exit: 1309
Dew point (ºC)	Sintering: -34 Rapid Cooling: No lecture.

APPENDIX 2: MICROINDENTATION HARDNESS

The microindentation hardnesses of T1 and T4 samples are grouped as ferrite and pearlite. When indenting the samples, the area of indentation (Mostly ferrite, more ferrite than pearlite, ferrite with pearlite, more pearlite than ferrite, mostly pearlite) was noted alongside the value. Anomalies and intermediate values (from areas with approximately 50% ferrite and 50% pearlite) have been eliminated, resulting in the following tables, Table 32 and Table 34.

Table 32: Microindentation hardness values for ferrite in T1 and T4.

Ferrite [HV]	**300 rpm**	158	170	170	174	176	176	176	177	177	181	181	185	186					
	1200 rpm	170	177	188	189	193	193	193	199	199	199	201	205	206	210	212	213	213	213

Table 33: ANOVA results for MH of ferrite.

ANOVA Ferrite [HV] (Alpha=0.05):	
Calculated F	Critical value F
34.34	4.18

An analysis of variance (ANOVA) reveals that the two series of values, 300 rpm (T1) and 1200 rpm (T4) are different from each other, as the calculated F value is higher than the critical value, as seen in Table 33.

Table 34: ANOVA results for MH of pearlite.

Pearlite [HV]	**300 rpm**	205	206	213	213	213	213	215	217	220	220	232	235	237								
	1200 rpm	220	220	225	225	228	228	228	230	232	235	235	237	237	237	237	237	240	245	245	247	254

Table 35: ANOVA results for MH of pearlite.

ANOVA Ferrite [HV] (Alpha=0.05):	
Calculated F	Critical value F
23.09	4.15

ANOVA for the pearlite MH also results in the two series of values, 300 rpm (T1) and 1200 rpm (T4) being different from each other, as seen in Table 35.

APPENDIX 3: OPTICAL AND ELECTRON MICROSCOPY

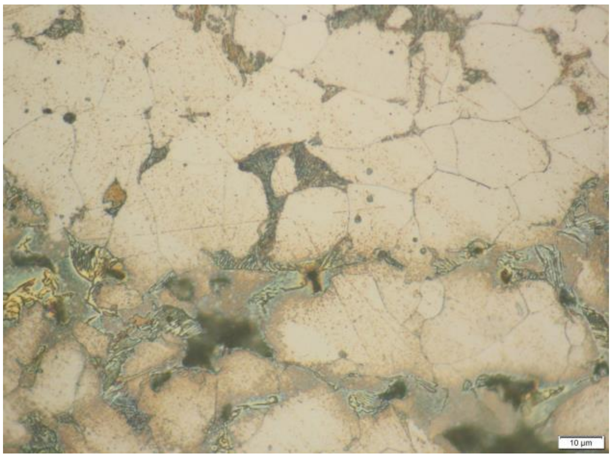

Figure 37: Micrograph of Ri.

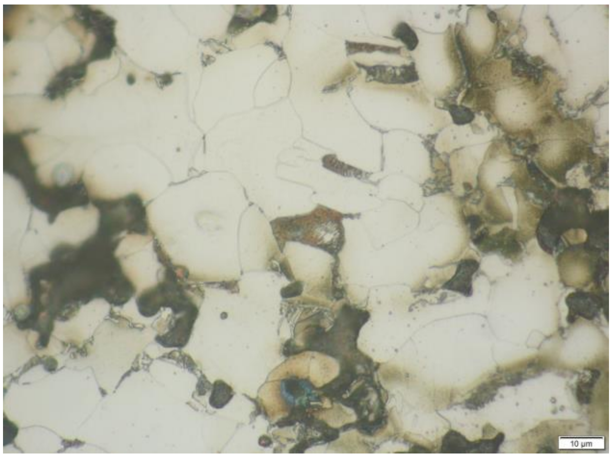

Figure 38: Micrograph of Riv.

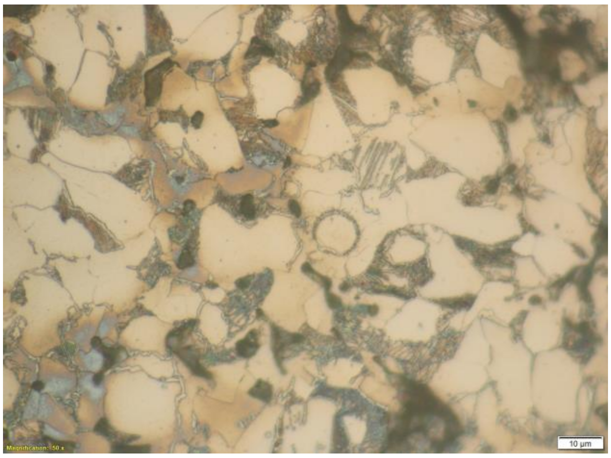

Figure 39: Micrograph of Ti.

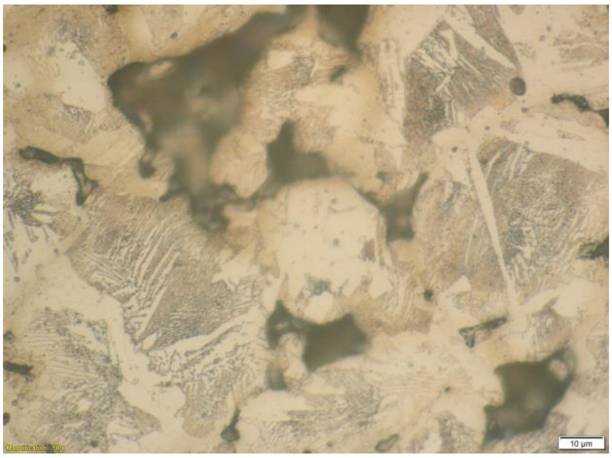

Figure 40: Micrograph of Tiv.

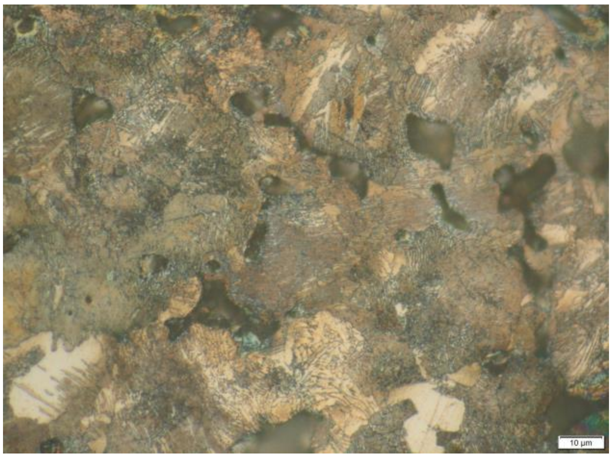

Figure 41: Micrograph of Si sample.

Figure 42: Micrograph of Siv sample.

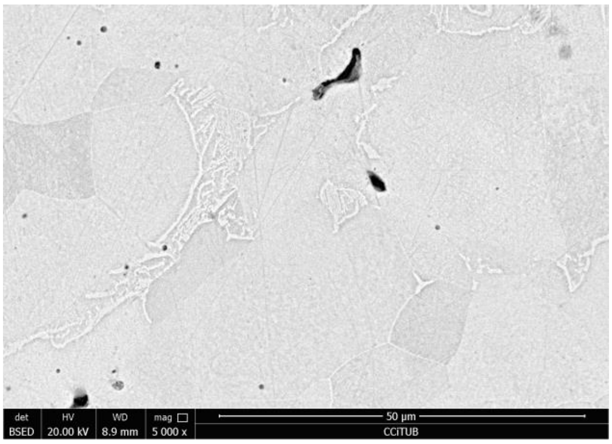

Figure 43: SEM Micrograph of Ri sample.

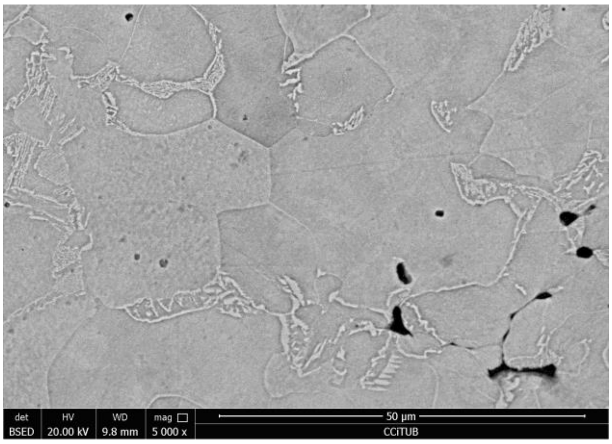

Figure 44: SEM Micrograph of Riv sample.

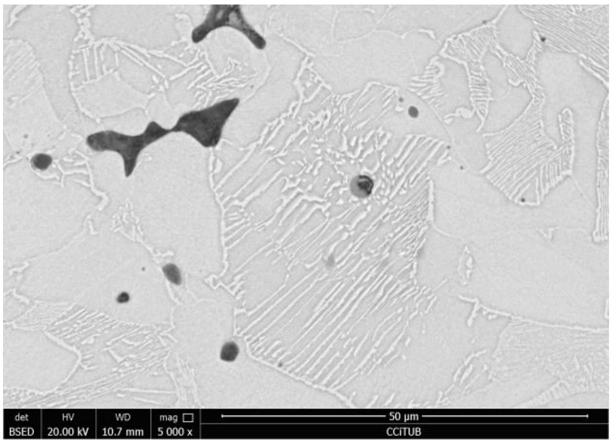

Figure 45: SEM Micrograph of Ti sample.

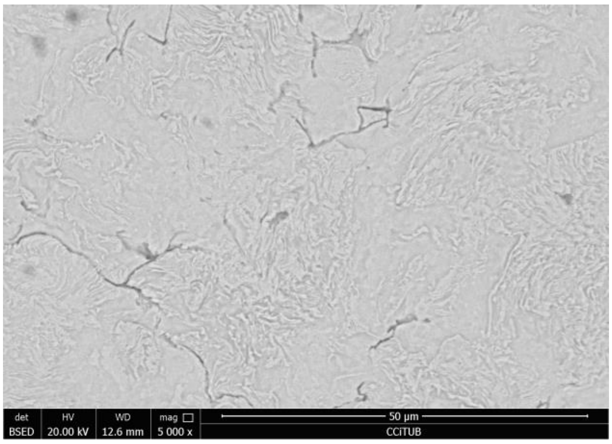

Figure 46: SEM Micrograph of unproperly polished Tiv sample.

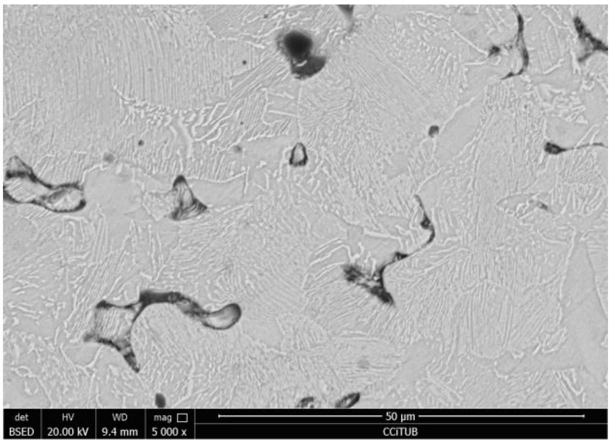

Figure 47: SEM Micrograph of Si sample.

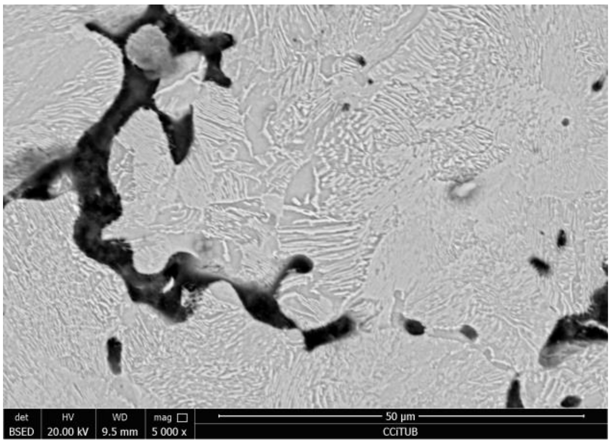

Figure 48: SEM Micrograph of Siv sample.